BIREFRINGENT DIRAC FERMION IN ANISOTROPIC VELOCITY MODULATED GRAPHENE JUNCTION

MR. EAKKARAT PATTRAWUTTHIWONG

A THESIS SUBMITTED IN PARTIAL FULFILLMENT OF THE REQUIREMENTS
FOR THE DEGREE OF MASTER OF SCIENCE (PHYSICS)
FACULTY OF SCIENCE
KING MONGKUT'S UNIVERSITY OF TECHNOLOGY THONBURI
2020

Birefringent Dirac Fermion in Anisotropic Velocity Modulated Graphene Junction

Mr. Eakkarat Pattrawutthiwong B.Sc. (Applied Physics)

A Thesis Submitted in Partial Fulfillment of the Requirements for
The Degree of Master of Science (Physics)
Faculty of Science
King Mongkut's University of Technology Thonburi
2020

Thesis Committee

..... Chairman of Thesis Committee
(Assoc. Prof. Bumned Soodchomshom , Ph.D.)

..... Member and Thesis Advisor
(Asst. Prof. Watchara Liewrian, Ph.D.)

..... Member
(Asst. Prof. Thana Sutthibutpong, Ph.D.)

..... Member
(Lect. Suwat Tangwancharoen, Ph.D.)

..... Member
(Lect. Tanapat Deesuwan, Ph.D.)

Thesis Title	Birefringent Dirac Fermion in Anisotropic Velocity Modulated Graphene Junction
Thesis Credits	12
Candidate	Mr. Eakkarat Pattrawutthiwong
Thesis Advisor	Asst. Prof. Dr. Watchara Liewrian
Program	Master of Science
Field of Study	Physics
Department	Physics
Faculty	Science
Academic Year	2020

Abstract

The tilt-mismatch effect on resonant tunneling through an electrical potential barrier in asymmetric tilt-Dirac cone junction is investigated. By varying barrier height, the angle-selective transmission of resonant tunneling oscillates as a function of gate voltage, and the linear phase shift due to the increase in the tilted parameter. We found that the signature of the tilt parameter can be determined by measuring the tunneling transport properties across the tilt-mismatch junction. For tilt-homogeneous junction, the tilt-induced pseudo-magnetic effect can occur only when an electric potential is applied to the system. However, the asymmetric tilt-energy dispersion systems also can mimic the pseudo-magnetic barrier structure without the electric potential. This result opens the opportunity for the tilt-Dirac cone system's magnetic focusing applications in electron-optics without magnetism.

Keywords : Tilted Dirac Cone / Pseudo-Magnetic Effect / Quantum Transport

ACKNOWLEDGEMENTS

I would like to gratefully thank my advisor Asst. Prof. Watchara Liewrian for his support and guidance throughout my master's studies. It was an invaluable experience working with him. I would like to thank the faculty of science, King Mongkut's University of Technology Thonburi for granting me the graduated level scholarship, and also the Thailand Center of Excellence in Physics for providing me the financial support on my research work. I appreciate the advices given by my colleagues and friends on both life and work. Finally, I am grateful to my family, who encourage me during this challenging period of my life.

CONTENTS

PAGE

LIST OF FIGURES

FIGURE **PAGE**

CHAPTER 1 INTRODUCTION

1.1 Background and motivation

Electronic transport in a two-dimensional (2D) system has been a popular topic in condensed matter physics since the first rise of Dirac material in 2004, known as graphene [1, 2]. Their novel transport properties arise from linear energy dispersion, where charge carriers mimic massless Dirac fermion (MDF) [3]. Graphene is one example of isotropic Dirac cone material, where energy dispersion around Dirac point has the same slope in k_x and k_y directions. However, theoretical studies revealed that graphene Dirac cone could exist in the tilted and anisotropic manner by band engineering. For example, by applying the periodic potential to graphene sheet, the anisotropy of Dirac cone can be tuned [4]. The DFT calculation predicted that hydrogenated graphene exhibits Dirac material with tilted anisotropic Dirac cones [5]. The nitrogen line defects in graphene are also predicted to induce type-II over-tilted Dirac cone [6]. Recently, it has been reported that the anisotropy of Fermi surface in high-T_c cuprate superconductors can be tuned by the hole doping [7]

In the last decade, great attention has been paid to investigate for new Dirac materials with anisotropic electronic properties. For example, two-dimensional stacked layers of phosphorene known as black phosphorus [8, 9] and bulk structure of $SrMnBi_2$ [10]. Recently, borophene, a 2D allotrope of boron, has successfully grown on silver surfaces and predicted to host anisotropic tilted MDF [11, 12]. Also, it's been reported that the anisotropy of high-Tc cuprate superconductors can be modulated by the hole doping [7]. Anisotropic and tilt of Dirac material offer some novel electronic properties; for example, the superconducting gap has been predicted to be enhanced during the phase transition between type-I and type-II cone in Weyl semimetal [13]. In the context of transport properties, it has been demonstrated that electron optic behaviors with the opposite chiralities refracted into opposite directions, which may be useful for valley filtering [14]. The tilted strength of a

Weyl semimetal combined with the magnetic field effect considerably enhances the conductance gap [15]. The potential barrier and tilt effect is also predicted to induce the pseudo-magnetic field resulting in the asymmetric transmission [16]. Therefore, it is beneficial to identify the tilted signatures of the Dirac cone to fine-tuning the electronic properties. In fact, It has been shown that the anisotropic tilted Dirac cone in $\alpha - (\mathrm{BEDT} - \mathrm{TTF})_2\mathrm{I}_3$ organic compounds can be measured by analyzing interlayer magnetoresistance [17]. Recently, It has been also demonstrated that the Fano factor is sensitive to the tilt of the cone and can be used to verify the tilted signatures of material [18].

In this work, the tunneling properties of electrons across the mismatch of the tilted Dirac cone are investigated. We first study the effect of the mismatch of the tilted Dirac cone on the electron transmission or resonance transmission in particular. We then analyze the tunneling resonance condition of electron and propose a method to measure the tilted strength of the Dirac cone. Moreover, we study the transmission under the influence of pseudo-magnetic field induced by the mismatch of the tilted Dirac cones

1.2 Objectives

1. To investigate the tunneling properties of Dirac electron through tilt-mismatch Dirac cone junctions.

2. To determine the resonance condition of electron tunneling that can be used to identify the tilted strength of the Dirac cone.

3. To design the tilt-mismatch Dirac material junction devices to indirectly measure the tilted strength of the Dirac cone.

4. To study the tunneling behaviors of electron under the influence of pseudo magnetic effect induced by the tilt-mismatch Dirac cone.

CHAPTER 2 THEORETICAL BACKGROUND

The first realization of Dirac material started in 1947 when P.R. Wallace proposed the band structure of graphite, or particularly graphene, using the tight binding method. At that time, the structure of few layer graphite (later called graphene) was not that popular, since the 2-dimensional crystal was thought to be unstable in normal condition. Until 2004, when Andre Geim and Konstantin Novoselov successfully extracted single-atom-thick crystallite graphene from bulk graphite [1]. This discovery changed how people think about the stability of 2-dimensional crystal structures and their popularity increased accordingly. It was pointed out that the electron in these materials exhibits massless Dirac particles rather than the usual Schrödinger Hamiltonian [3]. This class of materials is called "Dirac materials". The massless relativistic imitation of electron in Dirac materials leads to very high conductivity that is advantageous to high speed nanoelectronic application.

2.1 The electronic structure of Dirac materials

The tight binding method is commonly used to calculate the band structure of crystals. Graphene, for example, has a single layer of carbon atoms forming a perfect 2-dimensional honeycomb structure. three of four valence electrons of each carbon atom form sp^2 hybridized orbital and covalently bonded with the neighboring carbon atom. There is one electron left in $2p_z$ orbital, which is weakly bonded by the Van-der-Waals forces of carbon atom. Hence, these electrons are free to move or hop to other carbon atoms with little enough energy.

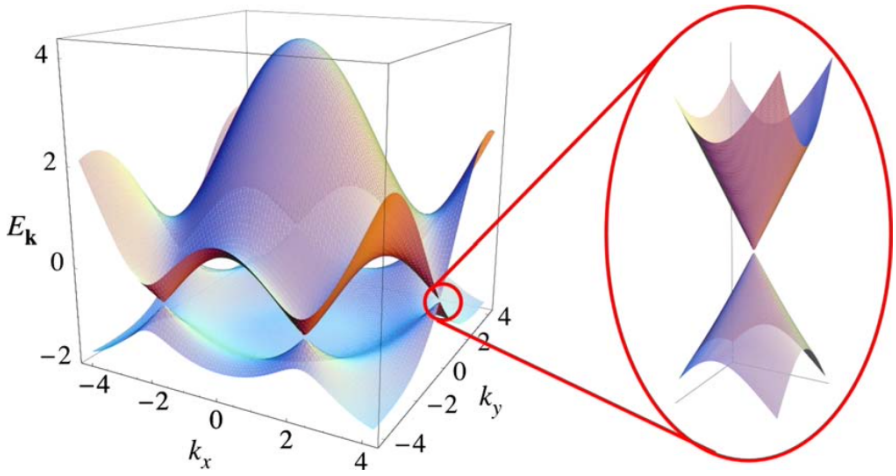

Figure 2.1 The energy dispersion of graphene. Left: the full band structure and right: the energy band close to one of the Dirac point [3].

The tight binding Hamiltonian for electron that can hop to both nearest-neighbor and next-nearest-neighbor atoms is given by

$$\begin{aligned} H = &- t \sum_{\langle\langle i,j\rangle\rangle,\sigma} (a^\dagger_{\sigma,i} b^\dagger_{\sigma,i} + \text{H.c.}) \\ &- t' \sum_{\langle\langle i,j\rangle\rangle,\sigma} (a^\dagger_{\sigma,i} a^\dagger_{\sigma,i} + b^\dagger_{\sigma,i} b^\dagger_{\sigma,i} + \text{H.c.}), \end{aligned} \tag{2.1}$$

where $t \approx 2.8$ meV is the nearest-neighbor hopping energy of electron, and t' is the next-nearest-neighbor hopping energy. $a^\dagger_{\sigma,i}$ and $b^\dagger_{b,i}$ are creation and annihilation operator, respectively. The eigenenergies of Hamiltonian above can be written as

$$\begin{aligned} E_F &= \pm t\sqrt{(3 + f(\boldsymbol{k}))} - t' f(\boldsymbol{k}), \\ f(\boldsymbol{k}) &= 2\cos(\sqrt{3}k_y a) + 4\cos\left(\frac{\sqrt{3}}{2}k_y a\right)\cos\left(\frac{3}{2}k_x a\right), \end{aligned} \tag{2.2}$$

where positive and negative sign correspond to the conduction and valence band. Fig. 2.1 show the full band structure of graphene with nonzero t and t'. Unlike parabolic dispersion relation of conventional semiconductors, the band structure of graphene close to one of the Dirac points is linear and gapless. This linear relation can be obtained analytically by applying the Taylor expansion to Eq. 2.2 about $q = 0$, where $q = k - K$ is relative wavevector measured from Dirac point

$$E_\pm(\boldsymbol{q}) \approx \pm v_F |\boldsymbol{q}| \tag{2.3}$$

where $v_F = 3ta/2 \approx 10^6$ m/s is Fermi velocity. The linear relation between energy and wavevector of an electron in the low-energy limit indicates that the electron

in graphene can be described by Dirac equation. In other words, the electron in graphene or Dirac material in general mimics massless relativistic particles.

2.2 The classification of Dirac cone materials

Dirac cones can be categorized according to the geometry of their Fermi surface. The conventional Dirac cone, like those found in graphene, has rotational symmetry about the momentum space. Their Fermi surface is closed and point-like at the band crossing, where the density of states vanishes as shown in Fig. 2.2a. However, they are not the only type of Dirac cone that can be found in Dirac materials. The general Dirac-like Hamiltonian of two dimensional system is given by

$$H(q) = (w_x q_x + w_y q_y)\sigma_0 + v_x q_x \sigma_x + v_y q_y \sigma_y, \tag{2.4}$$

where $q_{x,y}$ is the wave vector, v_x and v_y are Fermi velocity in the x- and y-direction, respectively. w_x and w_y represent the tilted velocities, σ_x and σ_y are Pauli matrices.

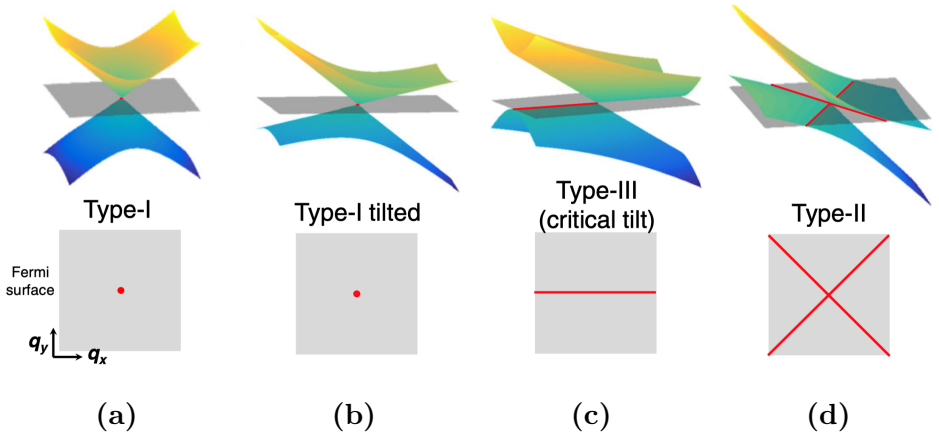

Figure 2.2 The types of Dirac cone and their corresponding Fermi surface with the zero-energy plane(grey). (a) Type-I Dirac cone characterized by the isotropy of wavevector k and a point-like Fermi surface. (b) Type-I tilted Dirac cone, which also has a point-like Fermi surface but the wavevector k is anisotropic. (c) Type-III Dirac cone with the straight line Fermi surface. (d) Type-II Dirac cone [19].

The eigenenergies of this Hamiltonian can be found as

$$E_{\pm}(q) = w_x q_x + w_y q_y \pm \sqrt{(v_x q_x)^2 + (v_y q_y)^2}. \tag{2.5}$$

If both coefficients w_x and w_y are zero, the Dirac cone is type-I. If w_x or w_y is nonzero, then the Dirac cone is tilted as shown in Fig. 2.2b. When the tilted parameter

$$w_0 = \sqrt{\left(\frac{w_x}{v_x}\right)^2 + \left(\frac{w_y}{v_y}\right)^2}, \tag{2.6}$$

is larger than 1, the Dirac cone is over-tilted and type-II Dirac point is formed. The Fermi surface of this type is two crossing lines, and the density of states becomes finite. When the tilted parameter $w_0 = 1$, the Dirac cone situates between the transition of type-I tilted and type-II Dirac cones. Due to their distinct Fermi surface, the Dirac cone of this kind has been named a type-III Dirac cone.

2.3 Borophene: A tilted anisotropic Dirac cone material

Graphene was the first one of its kind that successfully synthesized with high stability. This material class has been intensively studied due to their superiorly-high surface-volume ratio and novel electronic properties compared with bulk counterparts, one of which is the two-dimensional (2D) structure of borons. Boron compounds belong to the polyhedral class, which not only results in large variability of boron compound structures but also prevents the formation of flat covalent B-B bonding similar to graphene as shown in Fig. 2.3. Despite the potential application of boron-based 2D structure, this material faced a stability problem and its surface is chemically degraded in ambient conditions. This stability problem may be overcome by the introduction of intrinsic defects [20]. One of the most stable predicted structures of 2D phase of borons is $8 - Pmmn$ borophene. Their novel electronic properties were revealed by first-principles calculations, which predicted to be semimetallic with anisotropic and tilted Dirac cones [12, 21].

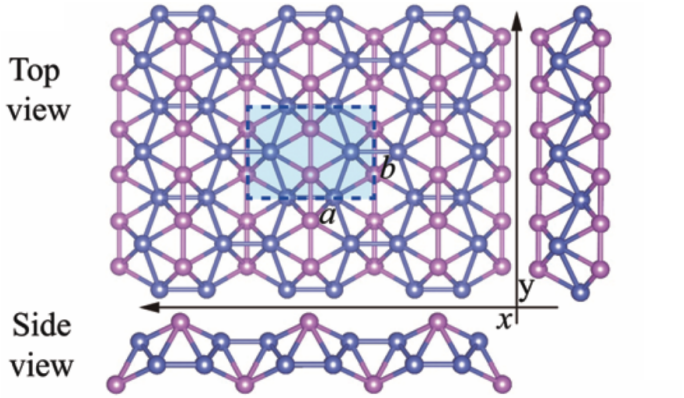

Figure 2.3 Atomic structure of $8-Pmmn$ borophene. The two different colors distinguish the two types of nonequivalent B atoms [22].

Recently, Atomically thin layers of borophene has been successfully grown on Ag(111) substrate using a solid boron atomic source under ultrahigh-vacuum conditions [11]. This experimental study was extended to the work on the synthesis of borophene-graphene heterostructures [23]. They have successfully integrated the borophene into 2D heterostructures with graphene (Fig. 2.4). Despite the mismatch of crystallographic lattices between borophene and graphene, the rich bonding configurations of boron achieved nearly atomically sharp lateral heterostructures. Unfortunately, the experimental realization of transport properties through these heterostructures has not yet been demonstrated. Which leaves plenty of room for improvement by the theoretical studies.

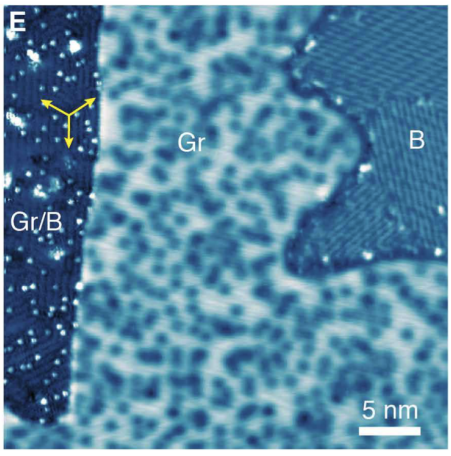

Figure 2.4 STM topography image of lateral and vertical heterostructures of borophene and graphene [23].

2.4 Klein tunneling effect in graphene

Klein tunneling refers to relativistic particles penetrate through the potential barrier without backscattering. These properties were once unique to the high-energy particles, where it can only be observed in the system with high-voltage-driven. In 2006, this effect is predicted to occur in low-energy systems of graphene [24]. This is because the electron in graphene mimics the relativistic massless Dirac particle and obey massless Dirac equation

$$\hat{H} = -i\hbar v_F \sigma \nabla \tag{2.7}$$

where $v_F \approx 10^6 \mathrm{ms}^{-1}$ is Fermi velocity, $\sigma = (\sigma_x, \sigma_y)$ is Pauli matrix.

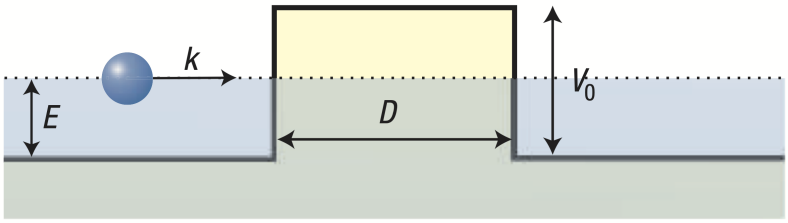

Figure 2.5 Schematic diagram of electron propagation through the potential barrier of height V_0 and width D [24].

The electron propagation can be modeled as in Fig. 2.5, consisting of three transport region where the Fermi energy of electron is below the potential barrier. By solving Eq. 2.7, the wave function of each region can be expressed as follows

$$\psi_1 = \begin{cases} (e^{ik_x x} + re^{-ik_x x})e^{ik_y y}, & x < 0, \\ (ae^{iq_x x} + be^{-iq_x x})e^{ik_y y}, & 0 < x < D, \\ te^{ik_x x + ik_y y}, & x > D, \end{cases}$$

$$\psi_2 = \begin{cases} s(e^{ik_x x + i\phi} - re^{-ik_x x - i\phi})e^{ik_y y}, & x < 0, \\ s'(ae^{iq_x x + i\theta} - be^{-iq_x x - i\theta})e^{ik_y y}, & 0 < x < D, \\ ste^{ik_x x + ik_y y + i\phi}, & x > D, \end{cases} \tag{2.8}$$

where $k_x = k\cos\phi$ and $k_y = k\sin\phi$ are x- and y-component wavevector outside the barrier region, respectively. $q_x = \sqrt{(E - V_0)^2/(\hbar v_F)^2 - k_y^2}$ is x-component wavevector inside the barrier region. $s = \mathrm{sgn}(E)$ and $s' = \mathrm{sgn}(E - V_0)$. Since the wave

function of each region has to be continuous at the boundary, we can substitute $x = 0$ and $x = D$ to Eq. 2.8, which give

$$\begin{aligned} 1 + r - a - b &= 0 \\ s(e^{i\phi} - e^{-i\phi}r) - s\prime(e^{i\theta}a - e^{-i\theta}b) &= 0 \\ e^{iDq_x}a + e^{-iDq_x}b - e^{iDk_x}t &= 0 \\ s\prime(e^{iDq_x+i\theta}a - e^{-iDq_x-i\theta}b) - se^{iDk_x+i\phi}t &= 0 \end{aligned} \tag{2.9}$$

where r and t is the reflection and transmission coefficient, respectively. Which can be obtained by solving the system of equations above. The reflection coefficient has the following expression

$$r = 2ie^{i\phi}\sin(q_xD) \times \frac{\sin\phi - ss'\sin\theta}{ss'[e^{-iq_xD}\cos(\phi+\theta) + e^{iq_xD}\cos(\phi-\theta)] - 2i\sin(q_xD)} \tag{2.10}$$

Since $T = |t|^2 = 1 - |r|^2$, the transmission probability can be expressed as follow

$$T = \frac{\cos^2\phi}{1 - \cos^2(q_xD)\sin^2\phi} \tag{2.11}$$

Fig. 2.6 shows the polar plot of Eq. 2.11. At the incident angle $\phi = 0$, electron tunnels through the barrier with probability of one no matter the height of the potential barrier. This is the feature unique to massless Dirac fermion called Klein tunneling.

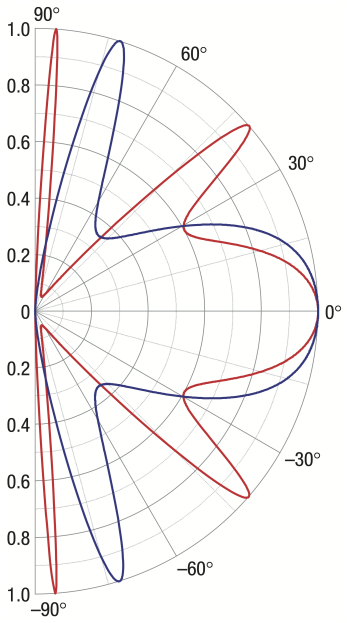

Figure 2.6 The transmission probability as a function of incident angle with different barrier height. $V_0 = 200$ meV for red curve and 285 meV for blue curve [24].

Moreover, Eq. 2.11 also results in perfect transmission at nonzero incident angles, which occurred under the resonance condition $q_x D = \pi N$, $N = 0, \pm 1, ...$ These perfect tunnelings are similar to Fabry-Perot interference in optics, where the incoming light rays constructively interfere with themselves inside the cavity. These angle-dependent transmissions were experimentally investigated in graphene heterojunctions [25]. The setup for measuring the angle-dependent transmission is shown in Fig. 2.7a. The measurement is carried out by applying the current bias between arm 1 and the other three arms, where the measurements are reported as the resistance of each arm as shown in Fig. 2.7b. These resistances can be measured using the standard four-probe technique.

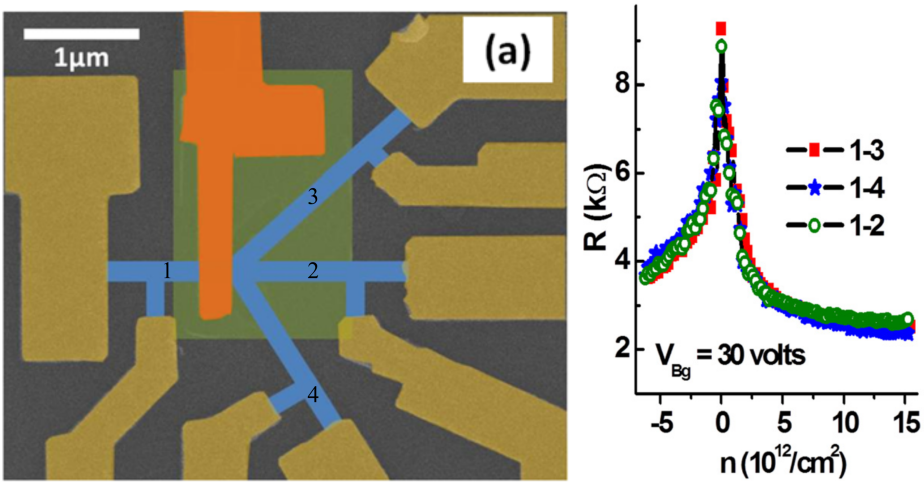

(a) **(b)**

Figure 2.7 (a) SEM image of single layer graphene device with straight and angles arms(blue). The angled arms are 45° with the straight arm. The bottom and top gates are shown in green and orange, respectively. The leads are shown in yellow. (b) Resistance as a function of carrier density under the application of top gate voltage for arms 2, 3, and 4. V_{Bg} is bottom gate voltage [25].

2.5 Electronic transport of electron in Weyl semimetals under the influence of magnetic field

In the previous section, we introduced the characteristic transport behavior of an electron in graphene such as the leakage of electron current due to the perfect tunneling at normal incident known as Klein tunneling. The discovery of graphene has enabled us to observe this uncommon effect in a condensed matter system [1]. The electron tunneling through the potential barrier has been studied both theoretically and experimentally [24, 25, 26]. In this section, we show the transport behavior of an electron in a 3-dimensional Weyl semimetal with the magnetic barrier.

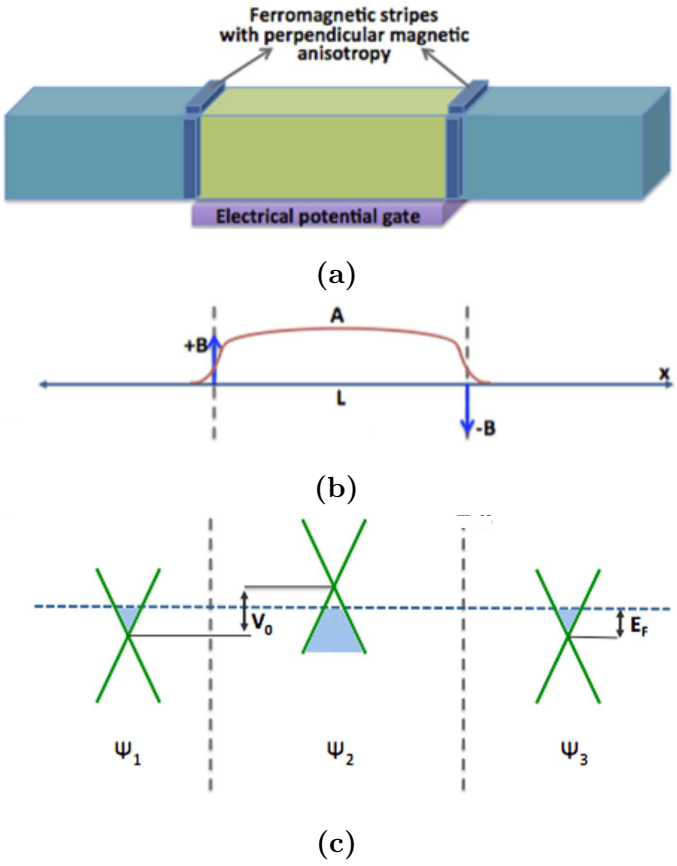

Figure 2.8 The schematic illustration of the single potential barrier Weyl semimetal under the influence of magnetic field induced by four ferromagnetic stripes on the top and one side surfaces [27].

The device structure is shown in Fig. 2.8a, where the delta-function magnetic fields at the barrier interfaces cause following gauge potentials on z- and y- directions

$$\begin{aligned} \vec{A}_{B_z} &= B_{0(z)} l_B [\Theta(x) - \Theta(x-L)]\hat{y} \\ \vec{A}_{B_y} &= B_{0(y)} l_B [\Theta(x) - \Theta(x-L)]\hat{z} \end{aligned} \tag{2.12}$$

where $l_B = \sqrt{\frac{\hbar}{|e|B_0}}$. Since the magnetic vector potential has an effect on electron momentum, the Hamiltonian of this system is given by

$$H = v_F(\sigma.(p + eA)) + V_0. \tag{2.13}$$

where v_F is the Fermi velocity, and σ is Pauli matrices. For simplicity, we consider Weyl electrons near one node and neglect the contribution of surface states and intervalley scattering. By considering the electron propagation along x-direction,

the eigenfunctions of Eq. 2.13 can be obtained as

$$\psi_{\pm} \equiv \frac{1}{\sqrt{2}} e^{ikr} \begin{pmatrix} 1 \\ e^{i\phi}\sec\gamma(\pm 1 + \sin\gamma) \end{pmatrix} \equiv \begin{pmatrix} \psi_a \\ \psi_b^{\pm} \end{pmatrix} \tag{2.14}$$

The ψ_a component for each regions in Fig. 2.8c can be written as

$$\begin{aligned} \Psi_{1,a}(x) &= e^{ik_x x} + re^{-ik_x x}, && x < 0, \\ \Psi_{2,a}(x) &= ae^{iq_x x} + be^{-iq_x x}, && 0 < x < L, \\ \Psi_{3,a}(x) &= te^{ik_x x}, && x > L. \end{aligned} \tag{2.15}$$

The ψ_b component can be found using the relation $\psi_2 = e^{i\phi}\sec\gamma(s+\sin\gamma)\psi_1$, where $s = \pm 1$ depending on the sign of energy $(E_F - V_0)$

$$\begin{aligned} \Psi_{1,b}(x) &= e^{i\phi}\sec\gamma(1+\sin\gamma)e^{ik_x x} - re^{-i\phi}\sec\gamma(1+\sin\gamma)e^{-ik_x x}, && x < 0, \\ \Psi_{2,b}(x) &= ae^{i\theta}\sec\alpha(s+\sin\alpha)e^{iq_x x} - be^{-i\theta}\sec\alpha(s+\sin\alpha)e^{-iq_x x}, && 0 < x < L, \\ \Psi_{3,b}(x) &= te^{i\phi}\sec\gamma(1+\sin\gamma)e^{ik_x x}, && x > L. \end{aligned} \tag{2.16}$$

The Fermi wavevector is

$$k_F = \sqrt{k_x^2 + k_y^2 + k_z^2} \tag{2.17}$$

where $k_x = k_F\cos\gamma\cos\phi$, $k_y = k_F\cos\gamma\sin\phi$, $k_z = k_F\sin\gamma$. The x-component wavevector inside the barrier is

$$q_x = \sqrt{\left(\frac{E_F - V_0}{\hbar v_F}\right)^2 - k_y^2 - k_z^2} \tag{2.18}$$

The propagating angles inside the barrier can be found by considering the conservation of y- and z-component wavevectors

$$\begin{aligned} \theta &= \tan^{-1}\left(\frac{k_y}{q_x}\right) \\ \alpha &= \tan^{-1}\left(\frac{k_z}{q_x}\cos\theta\right) \end{aligned} \tag{2.19}$$

Since the effect of magnetic vector potential shifts the transverse wavevectors $k_y \to k_y + \frac{eA_{By}}{\hbar}$, $k_z \to k_z + \frac{eA_{Bz}}{\hbar}$, the wavevectors along these directions have to be recalculated with the contribution of magnetic field, which can be written as

$$\begin{aligned} k_y &= \frac{E_F\cos\gamma\sin\phi + \eta v_F\sqrt{|B_{0(y)}|\hbar|e|}}{\hbar v_F}, \\ k_z &= \frac{E_F\sin\gamma + \eta v_F\sqrt{|B_{0(z)}|\hbar|e|}}{\hbar v_F}, \end{aligned} \tag{2.20}$$

where $\eta = \pm 1$ depending on the sign of the magnetic field.

First consider the transmission profiles in Fig. 2.9 in the case of no applied magnetic field (blue curves). When V_0 is close to E_F, the Fermi level is very close to the Weyl node in the barrier region. Therefore, only the normal incident electron ($\gamma \approx 0$ and $\theta \approx 0$) or Klein tunneling, in particular, can be transmitted perfectly as shown in Fig. 2.9a. When V_0 is much greater than E_F, we also achieve the Klein tunneling effect but with the additional perfect transmissions. These perfect transmissions can be understood by the resonance condition of Fermi wavevector k_F and the barrier length L, which can be derived using the relation $q_x L = n\pi$,

$$L\sqrt{\left(\frac{E_F - V_0}{\hbar v_F}\right)^2 - k_F^2 \sin^2\gamma - k_F^2 \cos^2\gamma \sin^2\phi} = n\pi, \tag{2.21}$$

where $n = 0, \pm 1, \ldots$. When the resonance condition above is satisfied, the angular perfect tunneling occurred as shown in Fig. 2.9b. The number and shape of the perfect transmissions can be intuitively predicted since they are highly dependent on applied voltage and Fermi energy. When the magnetic barrier is applied to the system, the transmission profiles become asymmetric, where the direction of the shift depends on the direction of the magnetic barrier. The influence of the magnetic field or magnetic vector potential to be specific is actually shifts the Weyl cone in the transverse direction. For this reason, with enough magnetic field strength, The Klein tunneling will be destroyed as the red and brown curve in Fig. 2.9a.

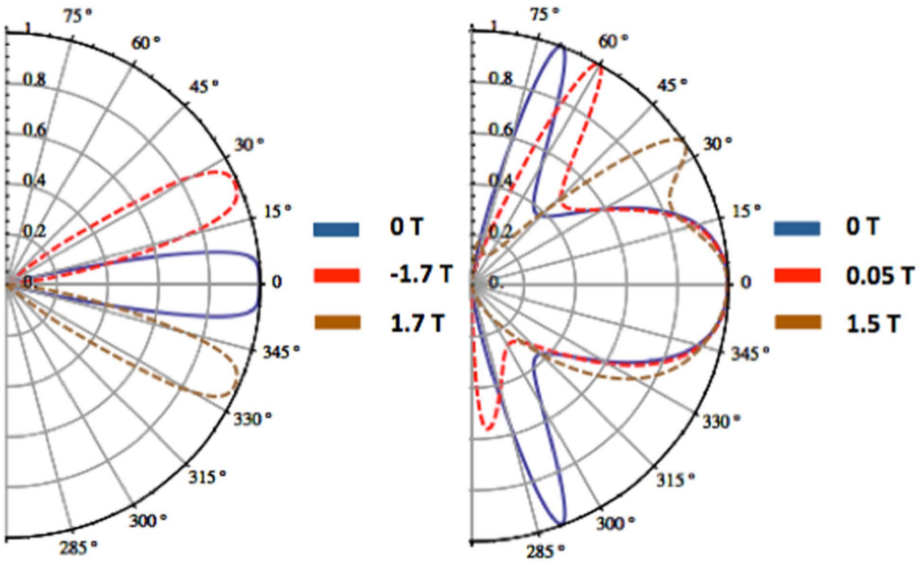

(a) **(b)**

Figure 2.9 The polar plot of transmission probabilities in the presence of different strength of applied magnetic barrier, where the angle between z-axis and xy-plane $\alpha = 0$. The potential barrier height is (a) 285 meV and (b) 63 meV, where the Fermi energy is 83 meV and barrier length is 100 nm [27].

2.6 Asymmetric tunneling of electron in tilted Weyl cone systems

The electronic structure of pristine graphene is often symmetric and non-tilted, which indicate that the transmission of electron is symmetric with respect to normal incident angle as shown in section 2.4. Unlike the Dirac cone of graphene, in 3-dimensional Weyl semimetals, the Weyl cone around the Weyl point is generally tilted and anisotropic as Weyl points are not located on high-symmetry k-points. A tilted Weyl fermion can be described by the low energy Weyl Hamiltonian with asymmetric velocities

$$H = V_0 + \sum_i \hbar k_i (\sigma^i v_i + w_i) \tag{2.22}$$

where σ^i are the Pauli matrices, v_i are the velocities in 3 dimensions, and V_0 is the potential barrier height. w_i is the tilt of Weyl cone in the unit of velocity. The model of interest is shown in Fig. 2.10 with the potential profile $V_{(x)} = V_0[\Theta(x) - \Theta(x - L)]$.

By solving the Hamiltonian above, the components of the wave functions are written as

$$\psi_{\pm} = \frac{1}{\sqrt{2}} e^{i\vec{k}\ \vec{r}} \begin{pmatrix} 1 \\ e^{i\phi} \sec\gamma(\pm 1 + \sin\gamma) \end{pmatrix} = \begin{pmatrix} \psi_a \\ \psi_b^{\pm} \end{pmatrix} \tag{2.23}$$

The transmission probability can be calculated by matching both components of the wave functions at the interfaces. The wave vector outside the potential barrier is expressed as

$$\begin{aligned} k_x &= k_F \cos\gamma \cos\phi, \\ k_y &= k_F \cos\gamma \sin\phi, \\ k_z &= k_F \sin\gamma \end{aligned} \tag{2.24}$$

and wave vector inside the potential barrier is

$$q_x = \frac{\sqrt{(E_F - V_0 - \hbar k_y w_y)^2 - \hbar^2 v_F^2 (k_y^2 + k_z^2)}}{\hbar v_F}. \tag{2.25}$$

The angles of electron propagation inside the potential barrier

$$\begin{aligned} \theta &= \arctan\left(\frac{k_y}{q_x}\right), \\ \alpha &= \arctan\left(\frac{k_z}{q_x}\cos\theta\right). \end{aligned} \tag{2.26}$$

can be calculated by considering the conservation of the transverse wave vectors k_y and k_z at the barrier interface $x = 0$.

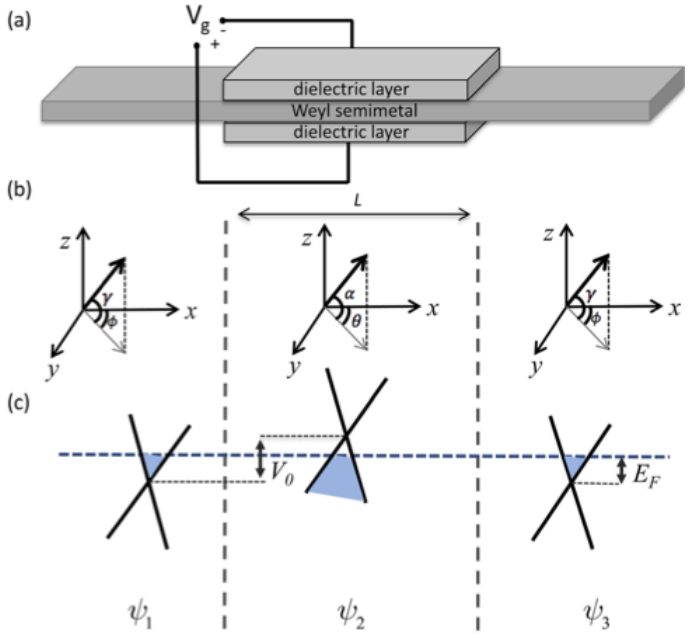

Figure 2.10 The schematic illustration of a Weyl semimetal under the influence of potential barrier of width L and height V_0 [16].

In the case of non-tilted Weyl cone system, the transmission probability is symmetric with respect to $\phi = 0$ and $\gamma = 0$ as shown in Fig. 2.12a. Which similar to the transmission of electron in graphene except that it is confined to two dimensions, whereas the Weyl semimetal is three dimensions. This symmetric transmission becomes asymmetric when the Weyl cone is tilted along with one of the transverse directions as shown in Fig. 2.12b. In other words, the transmission is shifted to the direction of the tilt. This can be understood by considering the Fermi surfaces in Fig. 2.11. In the case of $\phi > \phi_{a,b}$, q_x becomes imaginary since there is no state for electron to be occupied, therefore the electron is totally reflected. The shaded angles show the allowed range where the electron can propagate through the barrier. The analytical form of the critical angle of incident electron is found as

$$\phi_a = \sin^{-1}\left(-\frac{v_F(V_0 - E_F)}{E_F v_F - V_0 w_y}\right) \tag{2.27}$$

In the previous studies, the asymmetric transmission was only analyzed in the system with step magnetic or strain gauge potential [28, 29, 30]. Fig. 2.11b shows the Fermi surface under the influence of magnetic step vector potential $A_y = B_0 l_B \Theta(x)\hat{y}$, where $l_B = \sqrt{\frac{\hbar}{|e|B_0}}$, which was shifted by the amount of $k_y = k_y + \delta k_B$. In this case, the critical angle of incident electron is found as

$$\phi_b = \sin^{-1}\left(-\frac{V_0 - E_F + \eta v_F\sqrt{|B_0\hbar e|}}{E_F}\right) \tag{2.28}$$

where $\eta = \text{sign}(B_z)$. The equivalent y-component wavevector shifted due to the tilted Weyl cone and potential barrier can be approximately derived by considering the average of shift at the maximum and minimum points of k_y. By equating Eq. 2.27 and 2.28, the delta function pseudo-magnetic field generated by the application of potential barrier and tilted Weyl cone is given by

$$B \approx \frac{V_0^2 w_y^2}{e\hbar(w_y^2 - v_F^2)^2} \tag{2.29}$$

The transmission under the influence of magnetic vector potential is shown in Fig. 2.12f, where the magnetic field strength is calculated by Eq. 2.29 for $V_0 = 160$ meV and $w_y = 0.1 v_F$. The result almost identical to those of the tilted Weyl semimetal without the magnetic barrier (see Fig. 2.12b).

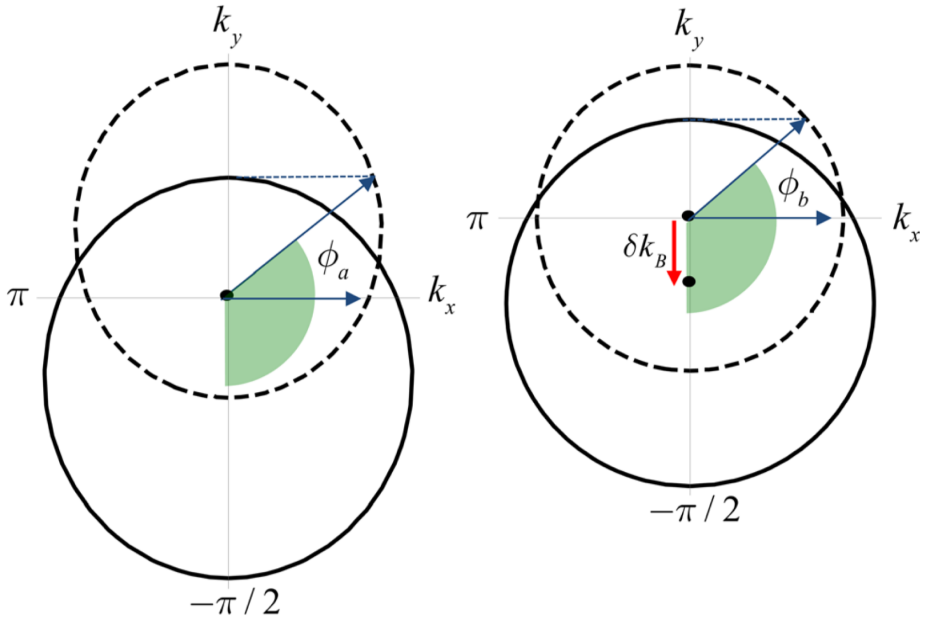

(a) **(b)**

Figure 2.11 The Fermi surfaces of Weyl cone in Fig. 2.10. The dashed (solid) line represents the Fermi surface in the absence (presence) of potential barrier, where Fermi energy $E_F = 82.6$ meV. (a) illustrate a tilted Weyl cone where $w_y = -0.4v_F$. (b) is the non-tilted Weyl cone under the influence magnetic gauge potential [16].

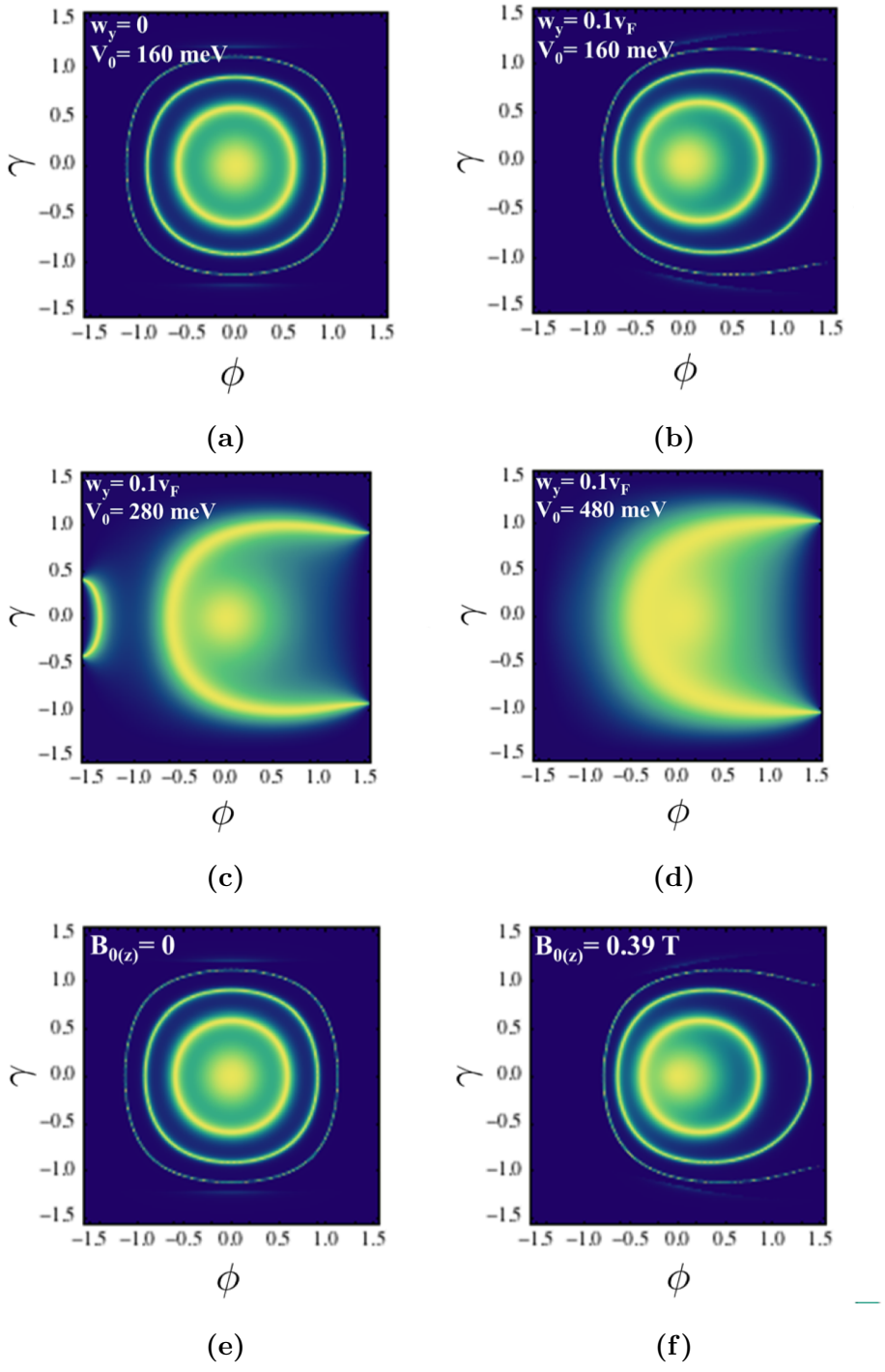

Figure 2.12 The contour plot of transmission probabilities with (a) non-tilted and (b)-(d) tilted by $w_y = 0.1v_F$ with the application of different potential barrier height in the middle region. (e) and (f) show the transmission probabilities of conventional non-tilted Weyl cone under the influence of different magnetic field strength B_z. Fermi energy $E_F = 82.6$ meV, the barrier length $L = 100$ nm for all configurations [16].

CHAPTER 3 MODEL AND METHOD

In this work, the tunneling properties of electrons across the mismatch of the tilted Dirac cone are investigated. We assume that the electron propagations are coherent and not affected by ohmic contact due to the heterogeneity of the junctions. The tunneling properties considered here are in low energy limit, in which the inter-valley scattering between K and K' in the Brillouin zone is negligible [31].

3.1 Tilt-mismatch Dirac cone junction

The proposed structure is depicted in Fig. 3.1, consisting of 2-dimensional Dirac material n-p-n heterojunctions with different tilted Dirac cones. To achieve such a device structure, the top gate is placed in the middle region of length L to tune the Fermi energy level, which can be realized by depositing Ti/Au using standard electron beam lithography [32]. Electrostatic doping using the ionic-liquid gate also has been demonstrated, which enhanced the carrier mobility [33]. For the barrier profile, we use rectangular potential barrier $U(x) = U[\Theta(x) - \Theta(x - L)]$.

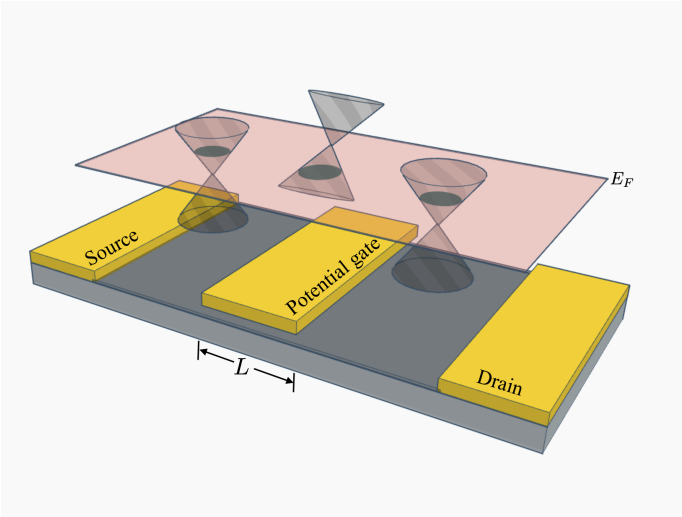

Figure 3.1 Schematic illustration of Dirac material n-p-n heterojunctions with the mismatch of Dirac cone. The position of Fermi energy level E_F can be controlled by tuning the voltage through potential gate of length L.

3.2 Transmission probability of electron in tilted Dirac cone

The wave function of Dirac electron in general Dirac materials can be obtain by solving the eigenvalue problem. Since the low-energy quasiparticles in Dirac material mimic relativistic particle, it can be described by effective massless Dirac Hamiltonian

$$\hat{H} = \hbar(v_F \sigma \cdot k + w\sigma_0 \cdot k) + U\sigma_0 \tag{3.1}$$

where U is barrier height, $v_F = 10^6$ ms^{-1} is Fermi velocity, $k = (k_x, k_y)$ is wave vector in the x-y plane, $\sigma = (\sigma_x, \sigma_y)$ is Pauli matrices, σ_0 is a 2×2 identity matrix, and $w = (w_x, w_y)$ is the parameter with the dimension of velocity denoting the tilt of Dirac cone. By solving Eq. 3.1, we obtain the wave function for each region as follows

$$\begin{aligned}
\psi_1 &= \begin{cases} e^{ik_x x} + re^{-ik_x x} & , x < 0 \\ s(e^{ik_x x}e^{i\phi} + re^{-ik_x x}e^{-i\phi}) & , x < 0 \end{cases} \\
\psi_2 &= \begin{cases} ae^{iq_x x} + be^{-iq_x x} & , 0 \le x < L \\ s'(ae^{iq_x x}e^{i\theta} - be^{-iq_x x}e^{-i\theta}) & , 0 \le x < L \end{cases} \\
\psi_3 &= \begin{cases} te^{ik_x x} & , x \ge L \\ ste^{ik_x x}e^{i\phi} & , x \ge L \end{cases}
\end{aligned} \tag{3.2}$$

The transmission coefficient t can be obtained by considering the continuity of the wave function at the boundaries $x = 0$ and $x = L$

$$\begin{aligned}
-a - b + r &= -1 \\
-sre^{-i\phi} - s'\left(ae^{i\theta} - be^{-i\theta}\right) &= -se^{i\phi} \\
ae^{iLq_x} + be^{-iLq_x} - te^{ik_x L} &= 0 \\
s'\left(ae^{i\theta + iLq_x} - be^{-i\theta - iLq_x}\right) - ste^{ik_x L + i\phi} &= 0
\end{aligned} \tag{3.3}$$

It is easier to solve for t using Cramer's rule. First put Eq. 3.3 into a matrix form, where each column from left to right contain the factor of the coefficient r, a, b, and t respectively.

$$\mathrm{M}_1 = \begin{pmatrix} 1 & -1 & -1 & 0 \\ -se^{-i\phi} & -s'e^{i\theta} & e^{-i\theta}s' & 0 \\ 0 & e^{iLq_x} & e^{-iLq_x} & -e^{ik_x L} \\ 0 & s'e^{i\theta + iLq_x} & -s'e^{-i\theta - iLq_x} & -se^{ik_x L + i\phi} \end{pmatrix} \tag{3.4}$$

Then, replace the column t with the factor on the right hand side of Eq. 3.3

$$\mathrm{M}_2 = \begin{pmatrix} 1 & -1 & -1 & -1 \\ -se^{-i\phi} & -s'e^{i\theta} & e^{-i\theta}s' & -se^{i\phi} \\ 0 & e^{iLq_x} & e^{-iLq_x} & 0 \\ 0 & s_p e^{i\theta+iLq_x} & -s'e^{-i\theta-iLq_x} & 0 \end{pmatrix} \tag{3.5}$$

The transmission coefficient t can be obtain from $t = \det \mathrm{M}_2 / \det \mathrm{M}_1$

$$t = \frac{2ss'\cos(\theta)\cos(\phi)(\sin(k_x L) + i\cos(k_x L))}{\sin(Lq_x)\,(s^2 - 2ss'\sin(\theta)\sin(\phi) + s'^2) + 2iss'\cos(\theta)\cos(\phi)\cos(Lq_x)} \tag{3.6}$$

The transmission probability can be obtained from $T = t^* t$

$$T = \frac{\cos^2\theta\cos^2\phi}{\cos^2(Lq_x)\cos^2\theta\cos^2\phi + \sin^2(Lq_x)(1 - ss'\sin\theta\sin\phi)^2} \tag{3.7}$$

3.3 The elliptic Fermi surface of tilted Dirac cone

When the Dirac cone is tilted, we obtain the elliptic Fermi surface in which the wavevector of electron is directional-dependent as shown in Fig. 3.2. In other word, the length of vector k varied as it rotate along the elliptic Fermi surface(dashed line). To understand relation between the electron wavevector and its incident angle ϕ, we consider the elliptic equation where the major axis of the ellipse is in y-direction.

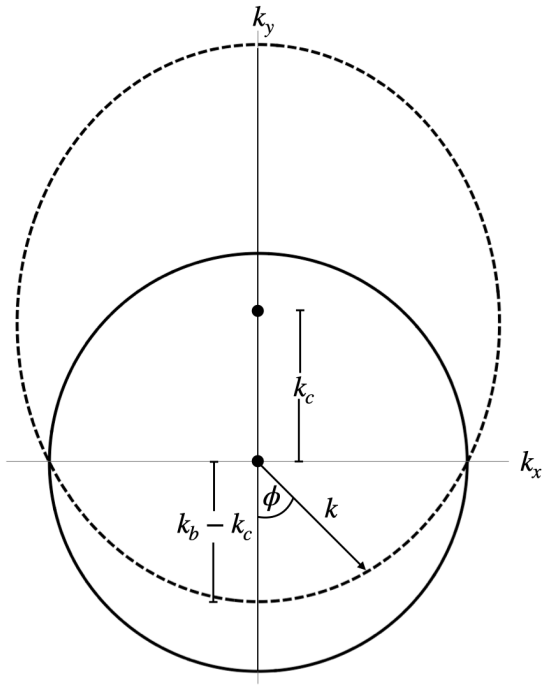

Figure 3.2 The cross-sectional area of non-tilted and tilted Dirac cone with $w_0 = 0.5$ represented by solid and dashed line, respectively.

$$\frac{k_x^2}{k_a^2} + \frac{k_y^2}{k_b^2} = 1 \tag{3.8}$$

where $k_x = k\cos\phi$ and $k_y = k\sin\phi + k_c$. Multiply both side with $k_a^2 k_b^2$ and substituting $\cos^2\phi = 1 - \sin^2\phi$

$$k_b^2 k^2 - k_b^2 k^2 \sin^2\phi + k_a^2 k^2 \sin^2\phi + 2k_a^2 kc\sin\phi + k_a^2 c^2) = k_a^2 k_b^2 \tag{3.9}$$

Since $k_a = k_b\sqrt{1-w_0^2}$ and $k_c = k_b w_0$ where w_0 is eccentricity of the ellipse, we obtain

$$\begin{aligned} &k_b^2 k^2 - k_b^2 k^2 \sin^2\phi + k_b^2(1-w_0^2)k^2\sin^2\phi \\ &+ 2k_b^2(1-w_0^2)kk_b w_0\sin\phi + k_b^2(1-w_0^2)k_b^2 w_0^2 = k_b^2(1-w_0^2)k_b^2 \end{aligned} \tag{3.10}$$

Multiplying both side with $-1/k_b^2$ and after some algebra, we obtain

$$k = \pm(kw_0\sin\phi - k_b(1-w_0^2)) \tag{3.11}$$

Since k is nonnegative, we have to choose the solution such that k is positive. Consider the case where $w_0 = 0$

$$k = \pm(-k_b)$$

We choose the negative solution in order for k to be positive.

$$\begin{aligned} k &= -kw_0\sin\phi + k_b(1-w_0^2) \\ k &= \frac{k_b(1-w_0^2)}{1+w_0\sin\phi} \end{aligned} \tag{3.12}$$

3.4 Angular dependent wavevector of tilted Dirac cone

We assume that the Dirac cone only tilted in y-direction. Therefore, the corresponding eigenenergy of Eq. 3.1 can be written as,

$$E_\eta = \hbar(\eta\sqrt{k_x^2 v_x^2 + k_y^2 v_y^2} + k_y w_y) + U \tag{3.13}$$

where η is band index. Since the tilt of Dirac cone determines the shape of Fermi surface in which the wave vector k is directional dependent. In order to see the form of wave vector under the effect of tilted Dirac cone, Eq. 3.13 can be rearranged to elliptic form as

$$\frac{k_x^2}{k_a^2} + \frac{(k_y + k_c)^2}{k_b^2} = 1 \tag{3.14}$$

where

$$k_a = \frac{(E_F - U)v_y}{\hbar v_x \sqrt{(\eta^2 v_y^2 - w_y^2)}}, k_b = \frac{\eta v_y (E_F - U)}{\hbar(\eta^2 v_y^2 - w_y^2)}, k_c = \frac{(E_F - U)w_y}{\hbar(\eta^2 v_y^2 - w_y^2)}$$

We have, in section 3.3, introduced the wavevector of electron as a function of incident angle ϕ. We can substitute k_b and k_c to Eq. 3.12, which gives

$$k = \frac{k_b(1 - w_0^2)}{1 + w_0 \sin\phi} = \frac{E_F - U}{\eta\hbar v_F(1 + w_0 \sin\phi)} \tag{3.15}$$

where

$$w_0 = \frac{k_c}{k_b} = \frac{(E_F - U)w_y}{\hbar(\eta^2 v_y^2 - w_y^2)} \frac{\hbar(\eta^2 v_y^2 - w_y^2)}{\eta v_y (E_F - U)} = \frac{w_y}{\eta v_F} \tag{3.16}$$

is tilted parameter and η is band index indicating that the conduction and valence band always tilted in the opposite direction. Eq. 3.15 is the angular dependent wavevector outside the barrier as a function of incident angle ϕ. Similarly, the wavevector inside the barrier region can be written as

$$q = \frac{E_F - U}{\eta\hbar v_F(1 + w_0 \sin\theta)} \tag{3.17}$$

where θ is the refracted angle of electron inside the barrier. This angle depends on the incident angle ϕ, which can be obtained by considering the conservation of transverse wavevector

$$\begin{aligned} q_y &= k_y \\ q\sin\theta &= k\sin\phi \\ \theta &= \sin^{-1}\left(\frac{k}{q}\sin\phi\right). \end{aligned} \tag{3.18}$$

Substitute θ that we derived above to Eq. 3.17, we obtain

$$q = \frac{E_F - U}{\hbar v_F s'} + \frac{w_0 k_y}{s'}, \tag{3.19}$$

and their x-component can be written as

$$\begin{aligned} q_x &= \sqrt{q^2 - q_y^2} \\ q_x &= \sqrt{\left(\frac{E_F - U}{\hbar v_F} + w_0 k_y\right)^2 - k_y^2}. \end{aligned} \tag{3.20}$$

CHAPTER 4 RESULT AND DISCUSSION

We start by investigating the tunneling properties of electron across tilted Dirac cone heterojunctions where we focus on how the effect of the gate potential and tilt affect the electron transmission. Then, we demonstrate a method to measure the tilted strength of the Dirac cone by identifying the tunneling behavior. Finally, we show that the transport behaviors of electron in tilted Dirac cone material are analogous to electron under the influence of magnetic field. We also show the derivation of magnetic field strength as a function of gate potential and tilted parameter.

4.1 Angular dependent of transmission probability

The transmission probabilities across the tilted Dirac cone heterojunctions under the variation of gate potential are presented in Fig. 4.1. The transmission profiles are symmetric in the case of $w_0 = 0$ regardless of the gate potential. When the tilted parameter is non-zero, the transmission profiles are shifted along the direction of the tilt and consequently become asymmetric, where the magnitude of the shift depends on the tilted strength of the Dirac cone. However, the presence of the tilt barely affects the tunneling profiles when the applied gate potential is close to the Fermi energy as shown in Fig. 4.1b. This is because the Fermi surface is small and the allowed wavevector states are narrowed. Therefore, electron propagations other than the normal incidence are backscattered.

Interestingly, when the applied gate voltage U is larger than the Fermi energy E_F, the transmission profiles exhibit peak tunneling as shown in Fig. 4.1c-d. These kind of tunnelings is called resonant tunneling, which occurred when the condition $q_x L = n\pi$, $n = 0, \pm 1, ...$ in Eq. 3.7 is met.

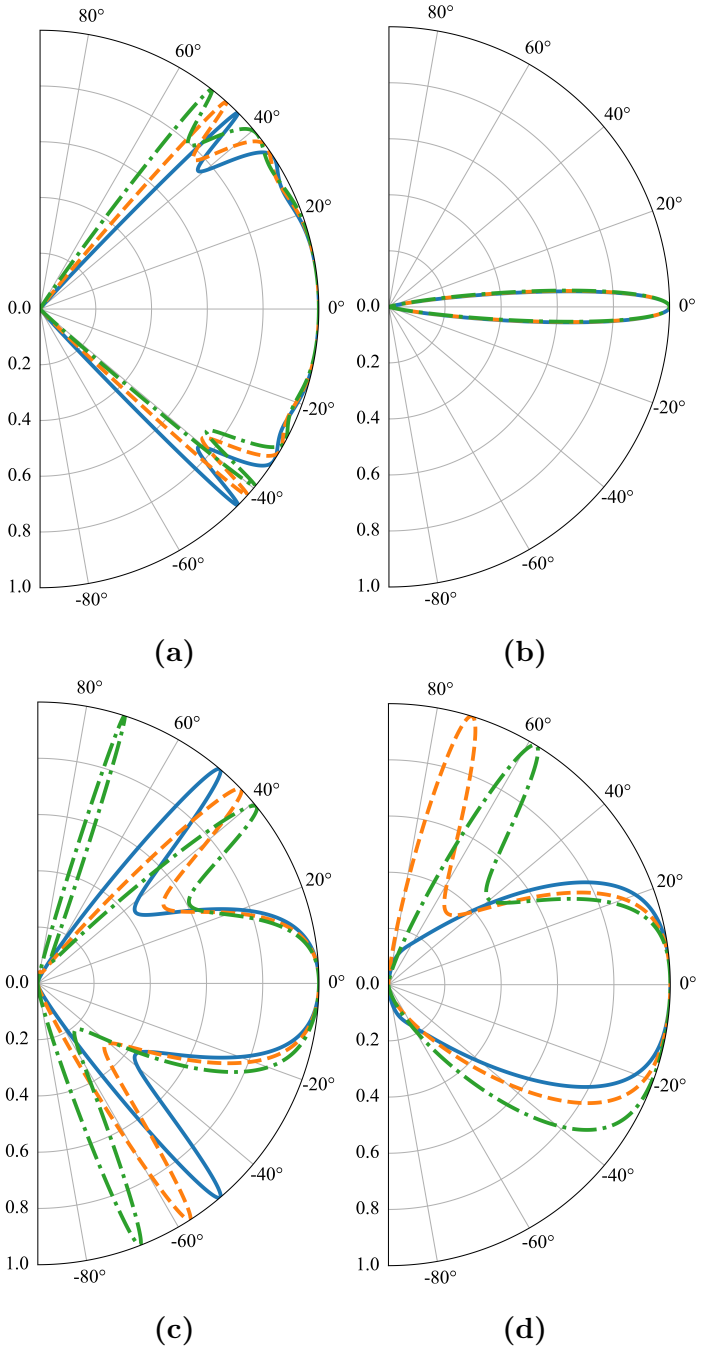

Figure 4.1 The polar plot of electron transmission probabilities for the tilted Dirac cone system with tilted parameter equal to 0 (solid line), 0.05 (dashed line), and 0.1 (dashed-dotted line). The applied gate voltage U is (a) 20, (b) 70, (c) 200, and (d) 285 meV. The Fermi energy $E_F = 80$ meV and barrier length $L = 100$ nm for all configurations.

4.2 The tilted strength identification by means of the tunneling resonance properties

The resonant tunnelings are arisen if the given U, E_F and, w_0 satisfy the resonance condition. Modulating these parameters result in shifting of resonant tunneling angles as previously reported in section 4.1. In this section, we demonstrate that by measuring the asymmetric resonant tunneling angles, the tilted parameter can be determined. Consider the resonance condition

$$L\sqrt{\left(\frac{E_F - U}{\hbar v_F} + w_0 k_y\right)^2 - k_y^2} = n\pi$$
$$w_{0\pm} = \frac{U - E_F}{\hbar v_F k \sin\phi} \mp \sqrt{1 + \left(\frac{n\pi}{kL\sin\phi}\right)^2} \tag{4.1}$$

where subscript $+(-)$ satisfy the positive(negative) angle ϕ region. One can obtain the tilted parameter by applying the gate voltage and Fermi energy then measure the resonant tunneling angle, which can be experimentally observed by four-point probes technique [25]. To illustrate how to calculate for the tilted parameter, we substitute the configuration of dashed-dotted line in Fig. 4.1c to Eq. 4.1. We choose the resonance condition $n = 4$, which corresponds to the resonant tunneling angle $\phi = 72^\circ$. We find $w_0 = 0.1$. Fig. 4.2 shows the contour plot of transmission probability, where each perfect transmission lines occur due to the different resonance conditions labeled by the integer n. These perfect transmission lines can be understood by analyzing Eq. 4.1. The position of perfect transmissions is determined by the term $\sqrt{(1 + (n\pi)^2/(k_y L)^2}$ since different value n give rise to different resonant tunneling conditions. For example, $\phi \approx -\pi/2$ the resonance condition $n = 6$ occur for $w_- \approx 0.34$, while in the case of $n = 7$, the tilted parameter $w_- \approx 0.57$. The term $(U - E)/\hbar v_F k_y$ is invariant under the resonance condition, therefore it is constant with different value n. This term determines the resonant tunneling profile and is responsible for distinctly different behaviors of resonance conditions $n = 5$ and 6, where w_0 decrease as ϕ go toward normal direction.

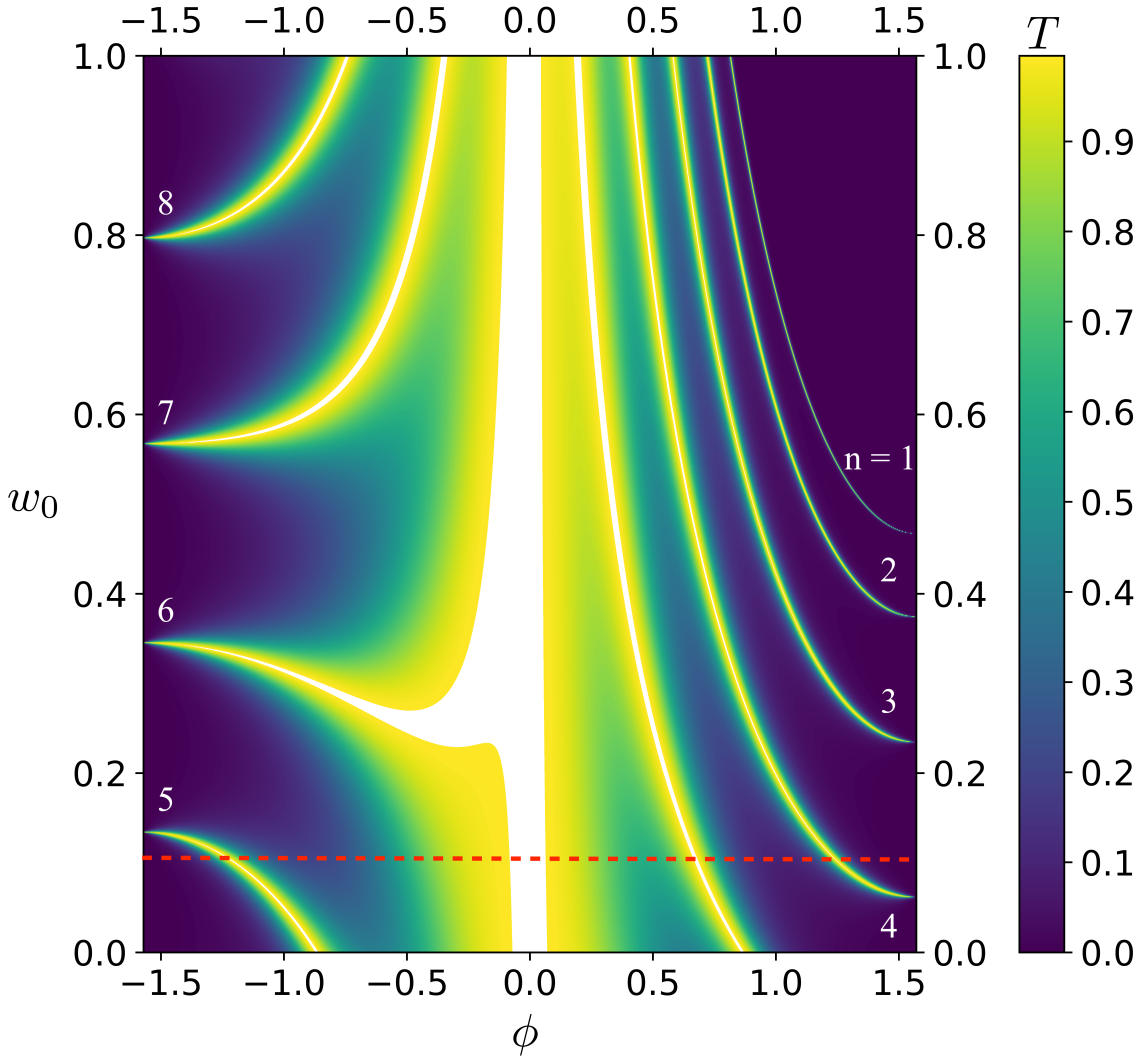

Figure 4.2 Contour plot of transmission probability. The Fermi energy $E_F = 80$ meV and gate potential $U = 200$ meV.

However, this method is not at all practical since the variable n is unlikely observable. Also, the only way to manipulate the electron propagations is by tuning the voltages through the bottom and top gate. In section 4.4, we propose a more practical method to identify the tilted strength, which again, involve with the resonant tunneling behaviors.

4.3 Oscillatory behavior of electron resonant tunneling

To understand the behaviors of resonant tunneling under the effect of the tilt and gate potential, we plot the transmission probabilities at fixed incident angle $\phi = 45°$ shown in Fig. 4.3. We found that the resonant tunneling oscillate with the increasing

of gate voltage where the voltage difference between each resonance condition is the same. Also The voltages required to satisfy the resonance conditions are increased with the tilted strength. These resonant tunnelings are shifted uniformly with the tilted parameter, which can be confirmed mathematically by taking the derivative to Eq. 4.1 with respect to U

$$\begin{aligned}\frac{dw_{0\pm}}{dU} &= \frac{d}{dU}\left(\frac{U-E_F}{\hbar v_F k\sin\phi} \mp \sqrt{1+\left(\frac{n\pi}{kL\sin\phi}\right)^2}\right) \\ &= \frac{1}{\hbar v_F k\sin\phi}.\end{aligned} \tag{4.2}$$

Eq. 4.2 indicates that the tilted parameter is linearly proportional to gate voltage.

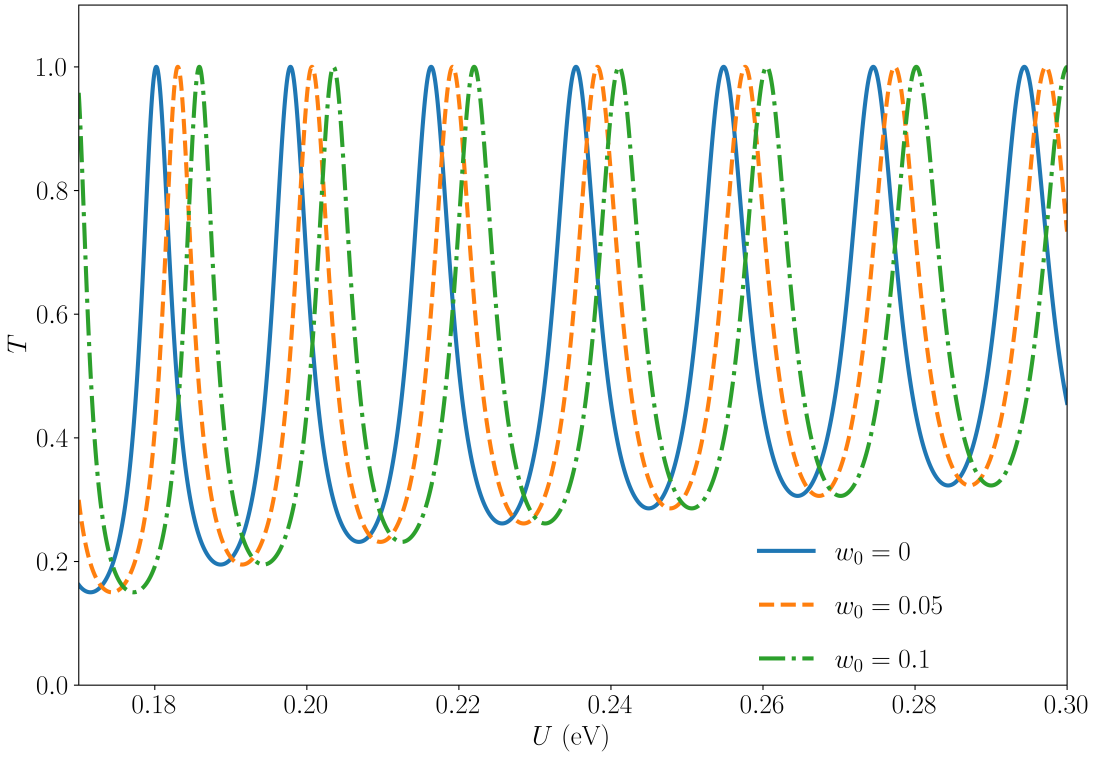

Figure 4.3 The transmission vs applied voltage at fixed tunneling angle $\phi = \frac{\pi}{4}$. Each perfect transmission corresponds to each resonance condition. The voltage difference between dashed-dotted and solid lines are the same for all resonance condition.

4.4 Revisit: The tilted strength identification by means of the tunneling resonance properties

In section 4.2, we have demonstrated a method to identify the character of Dirac cone using the resonant tunneling properties. The method can be applied to any resonance condition given that we have known its corresponding resonant tunneling angle. However, it is still not a practical method since the parameter n is unobservable. Also, most device configurations have fixed angled probes to observe the resonant tunneling current. In this section, we revisit this study again and eliminate the drawbacks mentioned above.

We have discussed earlier in section 4.3 that the relation of w_0 and U are linear with the slope of $1/\hbar v_F k \sin\phi$. For this reason, we can identify the tilted strength by measuring the difference between two voltages satisfied the same resonance condition.

$$\Delta w = \frac{\Delta U}{\hbar v_F k_y}. \tag{4.3}$$

To apply Eq. 4.3 to determine the tilted parameter, the voltages satisfied the same resonance condition have to be first determined, which can be achieved using the device structure depicted in Fig. 4.4a. We have to tune U until the resonant tunneling occurs at $\phi = \pi/4$, where the electron current can be measured as shown in Fig. 4.4b. The voltage at which the resonant tunneling occurs at $\phi = \pi/4$ for the case of non-tilted Dirac cone can be easily obtained since it is the system found in pristine graphene. Substituting these gate voltages to Eq. 4.3 we obtain $w_0 \approx 0.1$, which is the same value as dotted-dashed transmission profile in Fig. 4.4b.

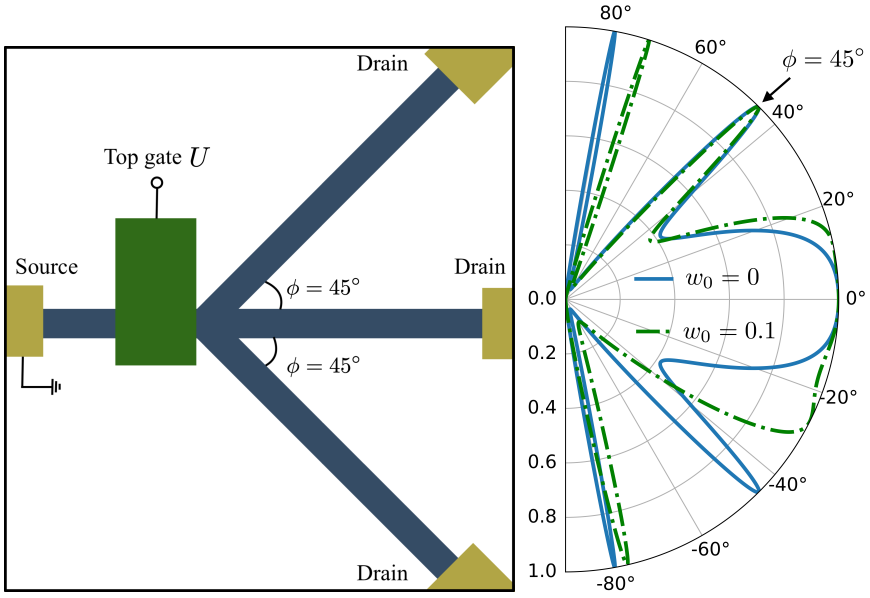

(a) **(b)**

Figure 4.4 (a) The device structure for the measurement of resonant tunneling electron. Straight blue lines represent the transport region where both arms are 45° angled with the normal direction. Green and yellow region represents top gate and electrode respectively. (b) Angular-dependent transmission for different applied voltages, $U = 180.2$ meV for solid line and $U = 185.85$ meV for dashed-dotted line. These voltages satisfy the resonance condition at $\phi = \frac{\pi}{4}$.

4.5 Tilt-induced transverse wavevector shift

In section 4.1, we have shown that the tunneling behavior of electron across the tilted Dirac cone exhibits asymmetric transmission. Previously, the transmission of this kind can be achieved by applying the magnetic barrier to the system [34, 35]. In this section, we demonstrate that the similar transmission profile can also be achieved in the tilted Dirac cone system without the magnetic barrier. Consider the x-component wavevector inside the barrier region $q_x = \sqrt{q^2 - k_y^2}$, which can be rearranged into the form

$$q_x \approx \sqrt{q'^2 - (k_y - q'w_0)^2} \tag{4.4}$$

where $q' = \frac{E_F - U}{\eta \hbar v_F}$. Notice that the y-component wavevector in Eq. 4.4 is shifted by the tilted Dirac cone similar to the wavevector shifted by the effect of magnetic vector

potential. Based on this analogy, we can derive the equivalent pseudo magnetic field

$$\begin{aligned} \frac{\xi}{l_B} &= -q' w_0 \\ \xi\sqrt{\frac{|e|B}{\hbar}} &= -\left(\frac{E_F - U}{\eta\hbar v_F}\right) w_0 \\ B &= \left(\frac{\varepsilon w_0}{v_F}\right)^2 \frac{1}{\xi\gamma\hbar|e|} \end{aligned} \tag{4.5}$$

where $\varepsilon = E_F - U$ is effective Fermi energy. $\xi = \pm 1$ is in fact the direction of magnetic field, but since these fields are induced by the tilted Dirac cone, it can be considered as the direction of the tilt. The positive(negative) sign mean that the Dirac cone tilted to the left(right) side with respect to normal direction. $\gamma = \pm 1$ indicate the carrier type in Fermi energy level. The typical strength of a tilt depends on the material themselves. For example, the DFT calculation results showed the tilted anisotropic Dirac cones in 6,6,12-graphyne with the strength $w_0 \approx 0.2$ [36, 37], which equivalent to the pseudo magnetic field strength $B_s \approx 0.88$ T under the effect of effective Fermi energy $\varepsilon = -120$ meV. Another Dirac material with tilted anisotropic Dirac cones is borophene. The first principle calculation revealed that the tilted parameter of 8-Pmmn borophene ≈ 0.3 [22], which can generate the pseudo magnetic field strength $B_s \approx 1.97$ T with $\varepsilon = -120$ meV.

4.6 The pseudo magnetic effect in the tilt-mismatch Dirac cone systems

We have found in section 4.5 that both the potential and tilt are the source of pseudo-magnetic field effect, where the strength and direction of the field can be controlled by tuning the effective Fermi energy. This effect actually been proposed in Weyl semimetal n-p-n junction with tilted Weyl cones [16]. However, the coupling of the tilt and top gate potential barrier is required to preserve the effect. In contrast to our work, where the top gate potential can be set to zero, and pseudo-magnetic field effect still occurred according to Eq. 4.5. Which is the consequence of the existence of the mismatch between Dirac cones with different tilted parameters. To show how the mismatch plays an important role in mimicking the pseudo-magnetic field effect without the requirement of potential barrier. We sketch the Fermi surface of the first and second regions, as shown in Fig. 4.5a, where top gate potential is

set to zero. Hence, electrons in both regions occupy in the same Fermi energy level. If the Dirac cones are tilted homogeneously, the Fermi surface of both regions are completely overlapped. Consequently, the electron can symmetrically propagate in all directions as shown in Fig. 4.5b. When the inhomogeneity is introduced, where only the Dirac cone in the second region is tilted while the first region is vertical non-tilted. The Fermi surfaces are partially overlapping as indicated by shaded area, which lead to asymmetric tunneling.

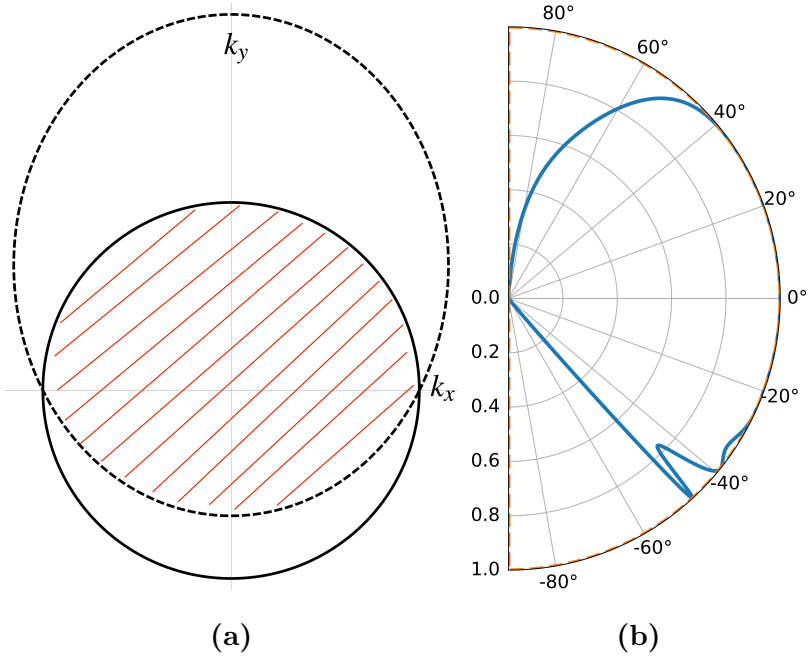

Figure 4.5 (a) The Fermi surfaces of Dirac cones in different regions. The solid line represents the Fermi surface of non-tilted Dirac cone in region I and the dashed line represents the Fermi surface of tilted Dirac cone $w_0 = 0.5$ in region II. (b) The transmission probabilities as a function of incident angle, where the solid (dashed) line is the case of the system with (without) the mismatch of Dirac cones. The Fermi energy $E_F = 80$ meV and gate potential is zero.

4.7 Transmission under the influence of pseudo magnetic field

To illustrate how pseudo magnetic field affects the tunneling behaviors compared to their real counterpart, the transmissions under the effect of pseudo and real magnetic fields are plotted as shown in Fig.4.6. First consider the case $U \gg E_F$, we found

that when the tilted parameter is small, the transmission profiles between the two systems are almost identical, as shown in Fig. 4.6a, which confirms the existence of pseudo-MVP. However, the pseudo-MVP is valid only if the strength of the tilt is small. Otherwise, the transmission profiles would become distinguishable, as shown in Fig. 4.6b. The same applies in the case of potential barrier $U = 0$, where the pseudo-MVP occurs when w_0 is small and becomes weak as w_0 increase as shown in Fig. 4.6c-d. Besides, the effect of real magnetic vector potential destroys the Klein tunneling, since it shifts the whole Dirac cone in momentum space. In contrast to pseudo magnetic vector potential, where momentum is also shifted but the position of Dirac point remains the same. As a result, the Klein tunneling is still preserved.

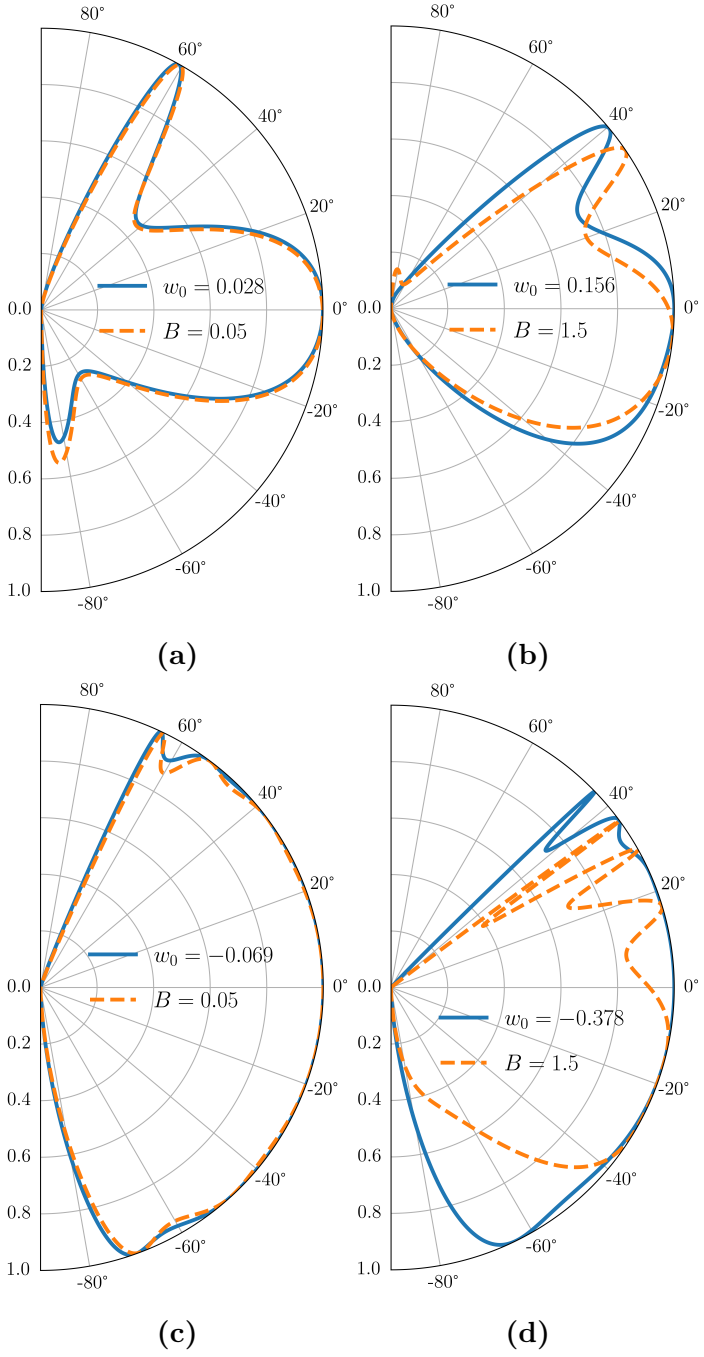

Figure 4.6 The polar plot of transmission probabilities as a function of incident angle of the system with tilted mismatch Dirac cone (solid line) and non-tilted system under the influence of delta magnetic field (dashed line). The Fermi energy $E_F = 83$ meV is the same for all plot, the gate potential $U = 285$ meV for (a) and (b), $U = 0$ for (c) and (d)

CHAPTER 5 CONCLUSION AND FUTURE WORK

5.1 Conclusion

The observation of electronic structure has been often performed by angle-resolved photoemission spectroscopy (ARPES), which is the standard method to investigate electronic properties of material. It has been suggested previously that the novel transport properties arise from anisotropy and tilt may be used to indirectly determine the character of Dirac cone [38]. Here we have shown that the asymmetric tunneling resonance can be utilized to verify the existence of the tilt. By tuning the appropriate voltage at the top gate, the tilted parameter can be determined. Which may be useful as an alternative method to study the electronic structure of materials. We also show that the electron transport behaviors across non-tilted/tilted/non-tilted heterostructure mimic the particle under the influence of real-magnetic field in non-tilted Dirac cone system. This study may be utilized for magnetic confinement applications such as magnetic waveguide. This device has been previously proposed where the stripes of ferromagnetic material are used to generate the MVP barrier. Which from the experimental point of view, implementing the ferromagnetic material into the device is quite challenging [39].

5.2 Future work

In this thesis, we presented several results that originate from the tilted energy dispersion of Dirac cones. For example, we can verify the tilted strength of Dirac cone by measuring the asymmetric tunneling properties of electron. We think that this result may be useful in the study of band structure of Dirac materials with tilted energy dispersion. We also pointed out that, despite the absence of gate potential, the pseudo magnetic field in a tilt-mismatch Dirac cone system still preserved. For this reason, the synthesis process would be even more simple since the application of voltage is not needed. We think that the tilt-induced pseudo magnetic field may be useful in the designing of magnetic devices without magnetism.

REFERENCES

1. K. S. Novoselov, A. K. Geim, S. V. Morozov, D. Jiang, 1 Y. Zhang, S. V. Dubonos, I. V. Grigorieva, A. A. F., 2004. "Electric Field Effect in Atomically Thin Carbon Films," **Science**, vol. 306, no. 5696, pp. 666–669.

2. Wehling, T. O., Black-Schaffer, A. M., and Balatsky, A. V., 2014. "Dirac materials," **Advances in Physics**, vol. 63, no. 1, pp. 1–76.

3. Castro Neto, A. H., Guinea, F., Peres, N. M., Novoselov, K. S., and Geim, A. K., 2009. "The electronic properties of graphene," **Reviews of Modern Physics**, vol. 81, no. 1, pp. 109–162.

4. Park, C. H., Yang, L., Son, Y. W., Cohen, M. L., and Louie, S. G., 2008. "Anisotropic behaviours of massless Dirac fermions in graphene under periodic potentials," **Nature Physics**, vol. 4, no. 3, pp. 213–217.

5. Lu, H. Y., Cuamba, A. S., Lin, S. Y., Hao, L., Wang, R., Li, H., Zhao, Y., and Ting, C. S., 2016. "Tilted anisotropic Dirac cones in partially hydrogenated graphene," **Physical Review B**, vol. 94, no. 19, pp. 1–7.

6. Zhang, H., Xie, Y., Zhong, C., Zhang, Z., and Chen, Y., 2017. "Tunable Type-I and Type-II Dirac Fermions in Graphene with Nitrogen Line Defects," **Journal of Physical Chemistry C**, vol. 121, no. 22, pp. 12476–12482.

7. Marino, E. C., Corrêa, R. O., Arouca, R., Nunes, L. H., and Alves, V. S., 2020. "Superconducting and pseudogap transition temperatures in high-Tc cuprates and the Tc dependence on pressure," **Superconductor Science and Technology**, vol. 33, no. 3.

8. Xia, F., Wang, H., and Jia, Y., 2014. "Rediscovering black phosphorus as an anisotropic layered material for optoelectronics and electronics," **Nature Communications**, vol. 5, pp. 1–6.

9. Kim, J., Baik, S. S., Ryu, S. H., Sohn, Y., Park, S., Park, B.-G., Denlinger, J., Yi, Y., Choi, H. J., and Kim, K. S., 2015. "Observation of tunable band gap and anisotropic Dirac semimetal state in black phosphorus," **Science**, vol. 349, no. 6249, pp. 723 LP – 726.

10. Park, J., Lee, G., Wolff-Fabris, F., Koh, Y. Y., Eom, M. J., Kim, Y. K., Farhan, M. A., Jo, Y. J., Kim, C., Shim, J. H., and Kim, J. S., 2011. "Anisotropic dirac fermions in a Bi square net of SrMnBi2," **Physical Review Letters**, vol. 107, no. 12, pp. 1–5.

11. Mannix, A. J., Zhou, X.-F., Kiraly, B., Wood, J. D., Alducin, D., Myers, B. D., Liu, X., Fisher, B. L., Santiago, U., Guest, J. R., Yacaman, M. J., Ponce, A., Oganov, A. R., Hersam, M. C., and Guisinger, N. P., 2015. "Synthesis of borophenes: Anisotropic, two-dimensional boron polymorphs," **Science**, vol. 350, no. 6267, pp. 1513 LP – 1516.

12. Zhou, X. F., Dong, X., Oganov, A. R., Zhu, Q., Tian, Y., and Wang, H. T., 2014. "Semimetallic two-dimensional boron allotrope with massless Dirac fermions," **Physical Review Letters**, vol. 112, no. 8, pp. 1–5.

13. Li, D., Rosenstein, B., Shapiro, B. Y., and Shapiro, I., 2017. "Effect of the type-I to type-II Weyl semimetal topological transition on superconductivity," **Physical Review B**, vol. 95, no. 9, pp. 1–9.

14. Nguyen, V. H. and Charlier, J. C., 2018. "Klein tunneling and electron optics in Dirac-Weyl fermion systems with tilted energy dispersion," **Physical Review B**, vol. 97, no. 23.

15. Yesilyurt, C., Siu, Z. B., Tan, S. G., Liang, G., and Jalil, M. B., 2017. "Conductance modulation in Weyl semimetals with tilted energy dispersion without a band gap," **Journal of Applied Physics**, vol. 121, no. 24.

16. Yesilyurt, C., Siu, Z. B., Tan, S. G., Liang, G., Yang, S. A., and Jalil, M. B., 2017. "Anomalous tunneling characteristic of Weyl semimetals with tilted energy dispersion," **Applied Physics Letters**, vol. 111, no. 6.

17. Morinari, T., Himura, T., and Tohyama, T., 2009. "Possible verification of tilted anisotropic Dirac cone in α-(BEDT-TTF)2I3 using interlayer magnetoresistance," **Journal of the Physical Society of Japan**, vol. 78, no. 2, pp. 3–6.

18. Trescher, M., Sbierski, B., Brouwer, P. W., and Bergholtz, E. J., 2015. "Quantum transport in Dirac materials: Signatures of tilted and anisotropic Dirac and Weyl cones," **Physical Review B - Condensed Matter and Materials Physics**, vol. 91, no. 11, pp. 1–6.

19. Milićević, M., Montambaux, G., Ozawa, T., Jamadi, O., Real, B., Sagnes, I., Lemaître, A., Le Gratiet, L., Harouri, A., Bloch, J., and Amo, A., 2019. "Type-III and Tilted Dirac Cones Emerging from Flat Bands in Photonic Orbital Graphene," **Physical Review X**, vol. 9, no. 3, pp. 1–11.

20. Liu, Y., Penev, E. S., and Yakobson, B. I., 2013. "Probing the synthesis of two-dimensional boron by first-principles computations," **Angewandte Chemie - International Edition**, vol. 52, no. 11, pp. 3156–3159.

21. Lopez-Bezanilla, A. and Littlewood, P. B., 2016. "Electronic properties of 8-Pmmn borophene," **Physical Review B**, vol. 93, no. 24, pp. 2–6.

22. Cheng, T., Lang, H., Li, Z., Liu, Z. Z., and Liu, Z. Z., 2017. "Anisotropic carrier mobility in two-dimensional materials with tilted Dirac cones: Theory and application," **Physical Chemistry Chemical Physics**, vol. 19, no. 35, pp. 23942–23950.

23. Liu, X. and Hersam, M. C., 2019. "Borophene-graphene heterostructures," **Science Advances**, vol. 5, no. 10, p. eaax6444.

24. Katsnelson, M. I., Novoselov, K. S., and Geim, A. K., 2006. "Chiral tunnelling and the Klein paradox in graphene," **Nature Physics**, vol. 2, no. 9, pp. 620–625.

25. Rahman, A., Guikema, J. W., Hassan, N. M., and Marković, N., 2015. "Angle-dependent transmission in graphene heterojunctions," **Applied Physics Letters**, vol. 106, no. 1.

26. Allain, P. E. and Fuchs, J. N., 2011. "Klein tunneling in graphene: Optics with massless electrons," **European Physical Journal B**, vol. 83, no. 3, pp. 301–317.

27. Yesilyurt, C., Tan, S. G., Liang, G., and Jalil, M. B., 2016. "Klein tunneling in Weyl semimetals under the influence of magnetic field," **Scientific Reports**, vol. 6, no. August, pp. 1–10.

28. Pereira, V. M. and Castro Neto, A. H., 2009. "Strain Engineering of Graphene's Electronic Structure," **Physical Review Letters**, vol. 103, no. 4, pp. 1–4.

29. Fujita, T., Jalil, M. B., and Tan, S. G., 2010. "Valley filter in strain engineered graphene," **Applied Physics Letters**, vol. 97, no. 4, pp. 2012–2015.

30. Wu, Z., Peeters, F. M., and Chang, K., 2010. "Electron tunneling through double magnetic barriers on the surface of a topological insulator," **Physical Review B - Condensed Matter and Materials Physics**, vol. 82, no. 11, pp. 1–7.

31. Abergel, D. S. and Chakraborty, T., 2009. "Generation of valley polarized current in bilayer graphene," **Applied Physics Letters**, vol. 95, no. 6, pp. 10–13.

32. Huard, B., Sulpizio, J. A., Stander, N., Todd, K., Yang, B., and Goldhaber-Gordon, D., 2007. "Transport measurements across a tunable potential barrier in graphene," **Physical Review Letters**, vol. 98, no. 23, pp. 8–11.

33. Perera, M. M., Lin, M. W., Chuang, H. J., Chamlagain, B. P., Wang, C., Tan, X., Cheng, M. M. C., Tománek, D., and Zhou, Z., 2013. "Improved carrier mobility in few-layer MoS2 field-effect transistors with ionic-liquid gating," **ACS Nano**, vol. 7, no. 5, pp. 4449–4458.

34. Ramezani Masir, M., Vasilopoulos, P., Matulis, A., and Peeters, F. M., 2008. "Direction-dependent tunneling through nanostructured magnetic barriers in graphene," **Physical Review B - Condensed Matter and Materials Physics**, vol. 77, no. 23, pp. 1–11.

35. Ramezani Masir, M., Vasilopoulos, P., and Peeters, F. M., 2010. "Fabry-Pérot resonances in graphene microstructures: Influence of a magnetic field," **Physical Review B - Condensed Matter and Materials Physics**, vol. 82, no. 11, pp. 1–12.

36. Malko, D., Neiss, C., Viñes, F., and Görling, A., 2012. "Competition for graphene: Graphynes with direction-dependent dirac cones," **Physical Review Letters**, vol. 108, no. 8, pp. 1–4.

37. Wang, Z., Zhou, X. F., Zhang, X., Zhu, Q., Dong, H., Zhao, M., and Oganov, A. R., 2015. "Phagraphene: A Low-Energy Graphene Allotrope Composed of 5-6-7 Carbon Rings with Distorted Dirac Cones," **Nano Letters**, vol. 15, no. 9, pp. 6182–6186.

38. Zhang, S. H. and Yang, W., 2018. "Oblique Klein tunneling in 8-Pmmn borophene p-n junctions," **Physical Review B**, vol. 97, no. 23, pp. 1–7.

39. Awschalom, D. and Samarth, N., 2009. "Spintronics without magnetism," **Physics**, vol. 2.

APPENDIX A

Mathematica Notebook

```
ψ1[x_] := (E^(I*kx*x) + r*E^(-I*kx*x));
ψ2[x_] := s (E^(I*kx*x)*E^(I*ϕ) - r*E^(-I*kx*x)*E^(-I*ϕ));
ψ3[x_] := (a*E^(I*qx*x) + b*E^(-I*qx*x));
ψ4[x_] := sp (a*E^(I*qx*x)*E^(I*θ) - b*E^(-I*qx*x)*E^(-I*θ));
ψ5[x_] := (t*E^(I*kx*x));
ψ6[x_] := s (t*E^(I*kx*x))*E^(I*ϕ);
```

In[1]:=
```
eq1 = {ψ1[0] - ψ3[0] == 0}
eq2 = {ψ2[0] - ψ4[0] == 0}
eq3 = {ψ3[L] - ψ5[L] == 0}
eq4 = {ψ4[L] - ψ6[L] == 0}

M1 = ({
  {1, -1, -1, 0},
  {-s E^(-I ϕ), -sp (E^(I θ)) , sp E^(-I θ), 0},
  {0, E^(I L qx), E^(-I L qx), -(E^(I kx L)) },
  {0, sp (E^(
   I L qx + I θ)) , -sp E^(-I L qx - I θ), -s (E^(
   I kx L + I ϕ)) }
 });
```

In[5]:=
```
M2 = ({
  {1, -1, -1, -1},
  {-s E^(-I ϕ), -sp E^(I θ),
   sp E^(-I θ), -s E^(I ϕ)},
  {0, (E^(I L qx)), E^(-I L qx), 0},
  {0, sp (E^(I L qx + I θ)) , -sp E^(-I L qx - I θ), 0}
 });
T = FullSimplify [Det[M2] / Det[M1]]
```

Out[6]=
$$\frac{4\ s\ sp\ \text{Cos}[\theta] \times \text{Cos}[\phi]}{\text{Det}[M1]}$$

In[7]:=
```
TT = FullSimplify [(
  2 s sp Cos[θ] × Cos[ϕ] (I Cos[kx L] + Sin[kx L])) / (
  2 I s sp Cos[L qx] × Cos[θ] × Cos[ϕ] +
   Sin[L qx] (s^2 + sp^2 - 2 s sp Sin[θ] × Sin[ϕ])) * (
  2 s sp Cos[θ] × Cos[ϕ] (-I Cos[kx L] +
    Sin[kx L])) / (-2 I s sp Cos[L qx] × Cos[θ] × Cos[ϕ] +
   Sin[L qx] (s^2 + sp^2 -
     2 s sp Sin[θ] × Sin[ϕ]))](*Transmission  Probability *)
```

Out[7]=
$$\frac{4\ s^2\ sp^2\ \text{Cos}[\theta]^2\ \text{Cos}[\phi]^2}{4\ s^2\ sp^2\ \text{Cos}[L\ qx]^2\ \text{Cos}[\theta]^2\ \text{Cos}[\phi]^2 + \text{Sin}[L\ qx]^2\ \left(s^2 + sp^2 - 2\ s\ sp\ \text{Sin}[\theta] \times \text{Sin}[\phi]\right)^2}$$

```
ħ = 1.054571726 * 10^-34;
vF = 10^6;
E0[E01_] := E01 * 1.602 * 10^-3 * 10^-19
V0[V01_] := V01 * 1.602 * 10^-3 * 10^-19
U0[U01_] := U01 * 1.602 * 10^-3 * 10^-19
L[L1_] := L1 * 10^-9
s[E01_] := Sign[E0[E01]]
sp[E01_, V01_] := Sign[E0[E01] - V0[V01]]
ξ[B0_] := Sign[B0]
η[E01_, V01_] :=
 Sign[V0[V01] - E0[E01]] (*type of carrier in magnetic field*)
α[ec_] := Sign[ec]
w[E01_, V01_, B0_] :=
 ξ[B0] × η[E01, V01] × Sqrt[(ħ vF^2 1.602 * 10^-19 Abs[B0]) / (E0[E01] - V0[V01])^2]
PB[E01_, V01_, ec_] := (((E0[E01] - V0[V01]) ec) / vF)^2 * η[E01, V01] / (ħ 1.602 * 10^-19)
θ[E01_, V01_, B0_, ec_, ϕ_] := ArcSin[ky[E01, V01, B0, ϕ] / q[E01, V01, B0, ec, ϕ]]
q[E01_, V01_, B0_, ec_, ϕ_] :=
 (E0[E01] - V0[V01]) / (ħ vF sp[E01, V01]) + (ky[E01, V01, B0, ϕ] ec) / sp[E01, V01]
ky[E01_, V01_, B0_, ϕ_] := ((E0[E01]) Sin[ϕ]) / (ħ vF) + ξ[B0] × Sqrt[(Abs[B0] 1.602 * 10^-19) / ħ]
k[E01_] := E0[E01] / (ħ vF (s[E01]))
k1[E01_, V01_, ec_, ϕ_] := (E0[E01] - V0[V01]) / (ħ vF (sp[E01, V01] + ec Cos[Pi / 2 + ϕ]))
(*Use only for plotting fermi surface*)
k2[E01_, V01_, ec_, ϕ_] := (E0[E01] - V0[V01]) / (ħ vF (sp[E01, V01] + ec Cos[Pi / 2 + ϕ]))
qx[E01_, V01_, B0_, ec_, ϕ_] :=
 Sqrt[(q[E01, V01, B0, ec, ϕ])^2 - (ky[E01, V01, B0, ϕ])^2]
TP[E01_, V01_, B0_, L1_, ec_, ϕ_] := (Cos[θ[E01, V01, B0, ec, ϕ]]^2 × Cos[ϕ]^2) /
  (Cos[L[L1] × qx[E01, V01, B0, ec, ϕ]]^2 × Cos[θ[E01, V01, B0, ec, ϕ]]^2 × Cos[ϕ]^2 +
    Sin[L[L1] × qx[E01, V01, B0, ec, ϕ]]^2
     (1 - s[E01] × sp[E01, V01] × Sin[θ[E01, V01, B0, ec, ϕ]] × Sin[ϕ])^2)
ecpos[E01_, V01_, L1_, ϕ_, n_] := (V0[V01] - E0[E01]) / (k[E01] vF ħ Sin[ϕ]) -
  Sqrt[((n Pi) / (k[E01] × L[L1] × Sin[ϕ]))^2 + 1]
ecneg[E01_, V01_, L1_, ϕ_, n_] := (V0[V01] - E0[E01]) / (k[E01] vF ħ Sin[ϕ]) +
  Sqrt[((n Pi) / (k[E01] × L[L1] × Sin[ϕ]))^2 + 1]
```

CURRICULUM VITAE

NAME	Mr. Eakkarat Pattrawutthiwong
DATE OF BIRTH	26 April 1995
EDUCATIONAL RECORD	
HIGH SCHOOL	High School Graduation Kaen Nakhon Wittayalai School, 2014
BACHELOR'S DEGREE	Bachelor of Science (Applied Physics) King Mongkut's University of Technology Thonburi, 2018
MASTER'S DEGREE	Master of Science (Physics) King Mongkut's University of Technology Thonburi, 2020
SCHOLARSHIP	Graduated Level Scholarship, Faculty of Science, King Mongkut's University of Technology Thonburi, 2018
	Thailand Center of Excellence in Physics Grant numbers: ThEP-61-PHM-SUT4
PUBLICATION	Soodchomshom, B., Niyomsoot, K., Pattrawutthiwong, E, 2018, "Switching effects and spin-valley Andreev resonant peak shifting in silicene superconductor," Physica E: Low-dimensional Systems and Nanostructures ,Vol 97, No. 1386-9477, pp. 375-383.

Pattrawutthiwong, E., Choopan, W. and Liewrian, W., 2021, "Possible Verification of Tilt Mismatch in Asymmetric Dirac-Cone Systems Using Resonant Tunneling Properties," Physics Letters A, Vol 393, No. 0375-9601, pp.127154.